



Title	Broadband Interferometric Observation of Lightning Discharges from Space
Author(s)	Kikuchi, Hiroshi
Citation	大阪大学, 2013, 博士論文
Version Type	VoR
URL	<a href="https://hdl.handle.net/11094/27549">https://hdl.handle.net/11094/27549</a>
rights	
Note	

*The University of Osaka Institutional Knowledge Archive : OUKA*

<https://ir.library.osaka-u.ac.jp/>

The University of Osaka

I12 96437

Doctoral Dissertation

Broadband Interferometric Observation  
of Lightning Discharges from Space

Hiroshi Kikuchi

January 2013

Department of Information and Communications Technology  
Division of Electrical, Electronic and Information Engineering  
Graduate School of Engineering, Osaka University, Japan

# Doctoral Dissertation

## Broadband Interferometric Observation of Lightning Discharges from Space

Hiroshi Kikuchi

January 2013

Department of Information and Communications Technology  
Division of Electrical, Electronic and Information Engineering  
Graduate School of Engineering, Osaka University, Japan

# Preface

This thesis presents a study of a broadband interferometric observation of lightning discharges from space. The contents of the thesis are based on the results of our research during the Ph.D. course at the Division of Information and Communications Engineering, Graduate School of Engineering, Osaka University.

A well-developed thundercloud causes local downpours and tornadoes accompanied with the lightning discharge. The remote sensing for lightning discharges from space is useful for the short-term forecast of weather disasters over vast areas. In this thesis, I will focus on a space-borne VHF broadband interferometer. The VHF broadband interferometer makes it possible to visualize the propagation of lightning discharges with high temporal and spatial resolutions. However, it has a few drawbacks in that the observation range is narrow like 30~50 km and the results of measurement are easily affected by multipath effects such as the geographical feature and also the reflection and diffraction from buildings. The observation of lightning discharges from space is useful in order to solve the above problems. To realize the space-borne VHF broadband interferometer, it is necessary to study the process for developing a space-borne lightning radio observation system and learn the propagation characteristics of electromagnetic waves radiated from lightning. A VHF sensor carried by the Maito-1 satellite was developed for observing the lightning discharge from space.

In this thesis, the radio observational results with the VHF sensor are described and VHF wave propagation characteristics in the ionosphere are also discussed. This thesis consists of 6 chapters that are organized as follows.

Chapter 1 contains the introduction of this study, the explanation of the former investigations reported, the outline of the ground-based and space lightning observation systems and their problems. The objective and significance of using the space-borne VHF broadband interferometer compared with the former systems are described.

In Chapter 2, the specifications of the VHF sensor and the Maito-1

satellite in detail are described. The initial observational results indicate that the quality of the VHF sensor for the radio observation of lightning discharges can be verified.

In Chapter 3, the observation results using the VHF sensor are compared with the observations with the World Wide Location Network (WWLLN). The WWLLN receives the VLF waves radiated from the lightning discharges and locates the radiation sources. Here the coincidence rates between the VHF sensor and the WWLLN are reported from quantitative comparison temporally and spatially. And also, the estimation of the arrival direction of VHF waves is performed using group delay characteristics.

In Chapter 4, the discussion and new knowledge on the wave propagation characteristics in the ionosphere using the observational results by the VHF sensor are described. The change of the pulse width in the ionosphere is discussed. When electromagnetic waves propagate through the dispersive medium, the waveform is affected by the group delay. The pulse width grows wider in the dispersive medium because the short duration VHF pulse with lightning activity has the wide band frequency characteristic. The propagation simulation is conducted in order to understand the change of the waveform using the ionospheric model. The pulse pairs recorded by the VHF sensor are discussed. The pulse pairs having the time interval (30 ns~ 1  $\mu$ s) were quite different from the previous studies. The numerical calculation of the wave propagation in the ionosphere considering the effect of geomagnetism is performed. The result indicated that the pulse pairs were caused by the mode separation of wave propagation in the ionosphere.

In Chapter 5, the outline of global lightning and sprite measurements (GLIMS) mission is presented. In this mission, the estimation of the arrival direction of the lightning radiation source will be carried out using the VHF interferometer (VITF) which consists of two VHF sensors. The ionospheric effect on the determination of lightning source location using the VITF is discussed using the numerical ionospheric model.

In Chapter 6, the results obtained by this study are summarized.

# Acknowledgement

First, I would like to express my sincere gratitude to my supervisor, Professor Zen-Ichiro Kawasaki of Graduate School of Engineering, Osaka University, for his encouragement, valuable discussions, and meaningful advices throughout my studies. His many constructive comments and kind advices have greatly improved this work.

I am much indebted to Professor Kenichi Kitayama of Graduate School of Engineering, Osaka University, who has given me many insightful suggestions for the thesis as an official reviewer. I take pleasure in thanking Professors Tetsuya Takine, Noboru Babaguchi, Seiichi Sampei and Kyou Inoue of Graduate School of Engineering, and Takashi Washio of Institute of Scientific and Industrial Research, Osaka University, for providing thoughtful comments on this work.

I am deeply grateful to Associate Professor Tomoo Ushio of Graduate School of Engineering, Osaka University for helping me a lot to carry out this work.

I am very grateful to Associate Professor Takeshi Morimoto of Faculty of Science and Engineering, Department of Electric and Electronic Engineering, Kinki University for discussion about my research, especially observation technique.

I also take pleasure in thanking Assistant Professor Gwan Kim of Graduate School of Engineering, Osaka University for helping me a lot of advices for my work.

I would like to thank Assistant Professor Satoru Yoshida of Graduate School of Engineering, Osaka University for helping me a lot to carry out this work.

I am so much obliged to say thank you to all members of Kawasaki laboratory for their continuous encouragement and meaningful discussions. Special thanks go to Messrs. Yusuke Nikai and Ryutaro Tanaka.

Finally, I heartily thank my family. They have always been giving me a lot of encouragement, which enabled me to accomplish the thesis.



# Contents

<b>1</b>	<b>Introduction</b>	<b>1</b>
1.1	Lightning discharge process and electromagnetic radiation	1
1.2	Lightning location system	3
1.3	Objective and overview	5
<b>2</b>	<b>VHF sensor on the Maido-1 satellite</b>	<b>7</b>
2.1	Introduction	7
2.2	Maido-1 satellite and VHF sensor	7
2.2.1	Basic concept	7
2.2.2	Maido-1 satellite configuration	8
2.2.3	VHF sensor configuration	9
2.3	Observations	10
2.3.1	Procedures	10
2.3.2	Observation Period	11
2.4	Observation results	11
2.5	Conclusion	13
<b>3</b>	<b>Evaluation of VHF sensor observations</b>	<b>15</b>
3.1	Introduction	15
3.2	Datasets	15
3.2.1	VHF sensor	15
3.2.2	World Wide Lightning Location Network	16
3.3	Methodology	17
3.3.1	Coincidence rate	17
3.3.2	Estimation of arrival direction of EM waves	21
3.4	Results and discussion	21
3.4.1	Coincidence rate	21
3.4.2	Estimation of arrival direction of EM waves	25
3.5	Conclusion	27

---

<b>4</b>	<b>Analysis of VHF electromagnetic waveforms in the ionosphere</b>	<b>29</b>
4.1	Introduction	29
4.2	Change of the pulse width	
4.2.1	Numerical study	29
4.2.2	Discussion about the pulse width	34
4.3	Pulse pairs recorded by VHF sensor	
4.3.1	Characteristics of the pulse pairs	37
4.3.2	Numerical study	38
4.3.3	Discussion about the pulse pairs	41
4.4	Conclusion	44
<b>5</b>	<b>VHF broadband interferometer on the ISS</b>	<b>47</b>
5.1	Introduction	47
5.2	Observation Instruments on JEM-GLIMS	48
5.2.1	GLIMS mission	48
5.2.2	VHF Interferometer	50
5.3	Evaluation of the estimation error of VITF	52
5.3.1	Simulation of the ionospheric effect	52
5.3.2	Methodology	53
5.3.3	Results and discussion	55
5.4	Conclusion	59
<b>6</b>	<b>Conclusion</b>	<b>61</b>
	<b>List of Acronyms</b>	<b>63</b>
	<b>Bibliography</b>	<b>65</b>
	<b>List of Publications</b>	<b>73</b>

# Chapter 1

## Introduction

### 1.1 Lightning discharge process and electromagnetic radiation

Well-developed thunderclouds cause many weather disasters which kill many people. Heavy rain from thunderclouds can lead to floods and flash floods. Strong winds such as local downpours and tornadoes also damage homes, buildings and so on. It is difficult to provide real-time monitoring of these climatic phenomena within a relatively short time (for several minutes). The thundercloud also produces lightning discharges in most cases. The monitoring details of lightning discharges are useful to prevent the weather disasters.

Updrafts in a thunderstorm produce various types of frozen precipitation to form within a cloud. These precipitation particles are roughly classified into very small ice crystals and much larger pellets of snow and ice. The smaller ice crystals are carried upward toward the top of the clouds by the updrafts while the heavier and denser pellets are either suspended by the updrafts or start falling toward the ground. Collisions occur between the ice crystals and the pellets, and these collisions serve as the charging mechanism of the thunderstorm. The small ice crystals become charged positively while the pellets become charged negatively. As a result, the top of the cloud becomes positively charged and the middle to lower part of the storm becomes negatively charged. The charge structure in the thunder cloud causes lightning discharges. Lightning is a spark-like electrical discharge produced in thunderstorms. There are roughly two types that include the cloud-to-ground (CG) lightning and intracloud (IC) lightning. Observations have shown that the majority of lightning discharges are of type IC, however the magnitude of the involved current is much less than what is observed in CG lightning.

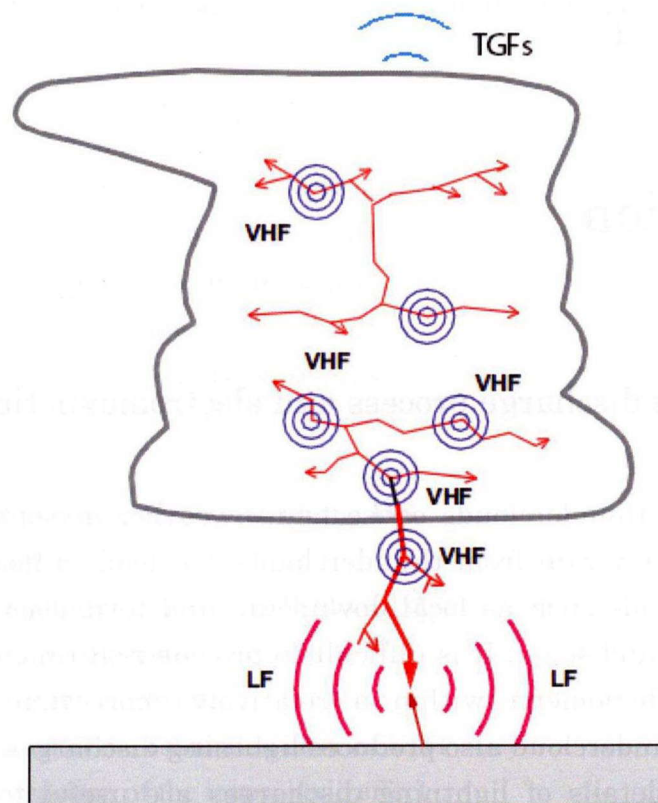


Fig. 1.1 Schematic of radiation from lightning. The return stroke of Cloud-to-Ground lightning emits strong LF radiation. Leader processes and recoil streamer in intracloud lightning generate predominately VHF radiation. TGFs are caused by electric fields produced above thunderstorms [1].

Lightning discharges produce electromagnetic radiation over a very wide frequency spectrum, from extremely low frequency (ELF: 3-30Hz) to Gamma-ray. The electromagnetic waves in the frequency range of ELF through low frequency (LF: 3-30 kHz) are mainly radiated from return strokes, as a result of the large amount of charge carried by return strokes. On the other hand, the radiation associated with IC lightning is produced by hundreds of very fast transient pulses radiating mainly in Very High Frequency (VHF: 30 - 300MHz). The terrestrial gamma-ray flashes (TGFs) are bursts of gamma rays in the Earth's atmosphere [2]. They are probably caused by electric fields produced above thunderstorms. Fig. 1.1 shows the illustration of radiation from lightning.

## 1.2 Lightning location system

Most of the lightning location systems are based on the detection of the electromagnetic radiation in the optical and radio range from lightning. Most of the ground based lightning location systems have used the electromagnetic waves in radio frequency ranges, which are in VHF or LF/VLF band.

The lightning location system using VHF sensors can visualize the lightning channels in either two or three dimensions. VHF networks normally consist of several stations separated by tens of kilometers. Each station detects radio frequency bursts in the frequency range in VHF band. While this method supplies great detail about lightning in individual thunderstorms, it cannot be used over large regional areas [3], [4], [5].

VLF sensors can be separated by hundreds to thousands of kilometers, while still being able to detect the VLF radiation emitted by individual lightning flashes, because the attenuation of the atmospheric radio waves at VLF frequencies (3-30 kHz) is lower than VHF waves. There are many regional networks using VLF band which have been installed all over the world [6], [7], [8]. The one disadvantage of using VLF sensors over large regions is that the sensors are sensitive primarily to vertically oriented lightning discharges such as return strokes, while the detection efficiency of these flashes depends on the spacing of the sensors. Hence, much of the horizontal IC discharges are not detected by these large scale networks. As a representative VLF lightning location system, the World Wide Lightning Location Network (WWLLN) is the only ground based observation system for the global lightning activity. Recent research indicates the detection efficiency for strokes about 50 kA is approximately 30% [9].

Recently the lightning observations using the satellite have been conducted. The following instruments are representative optical instruments. The Optical Transient Detector (OTD) was launched in 1995. The OTD has contributed to the discovery that the global flash rate is approximately 40 flashes per second, less than half of the widely accepted estimates dating back to 1925 [10]. The Lightning Imaging Sensor (LIS) was launched in 1997 to detect the distribution and variability of total lightning that occurred in the tropical regions of the globe [11]. While the optical observation using the

satellite is useful to monitor the global lightning activity, the detection efficiency of lightning is lower during the daytime (about 70 %) than during the nighttime (about 90 %).

The Fast On-orbit Recording of Transient Events (FORTE) satellite was also launched in 1997 and conducted the radio observations of the lightning discharges [12]. FORTE carried the radio observation payload which characterized pass band with 22-MHz channel placed in the range 26-48 MHz, with a nominal 38-MHz center, and the other in the range 118-140 MHz, with a nominal 130-MHz center. From the radio observation results, satellite-observed VHF emissions were much more likely to be associated with IC lightning than with CG lightning [13].

These lightning location systems have following assignments to consider the constantly lightning monitoring system over vast areas.

- The system using less than low frequency has a low sensitivity for IC lightning.
- The optical instrument has variable detection efficiency during day and night time. In general, it is lower at day time than at night time.
- The positioning technology of the lightning discharges using VHF waves from space has never achieved.

Lightning Research Group of Osaka University (LRG-OU) has been developing the ground-based VHF broadband digital interferometer (DITF) to image precise lightning channels and to monitor lightning activities. DITF is defined as the detection of both IC and CG lightning flashes. The remarkable feature of DITF is its ultra-wide bandwidth (from 30 MHz to 100 MHz) and implicit redundancy for estimating VHF source locations [14]. The observation range is several tens of kilometers. In general, the scale of the thundercloud is from several kilometers to several tens of kilometers. It is not enough to monitor the entire thundercloud activity.

I propose to observe the lightning discharges using the VHF DITF from space which terms 'the space-borne VHF DITF'. The space-borne VHF DITF makes it possible to monitor the lightning discharges in details over vast areas whether the observation area is in the day-and-nighttime.

### 1.3 Objective and overview

For some verification to realize the space-borne VHF DITF, the VHF sensor carried on the Maido-1 satellite was developed. It was proposed to examine the feasibility of broadband VHF lightning observations and also to learn the radio propagation characteristics through the ionosphere. It is necessary to study the ionospheric effect on the determination of lightning source location using VHF radio waves.

In this thesis, the radio observational results with the VHF sensor and the broadband VHF wave propagation characteristics in the ionosphere using the observation and numerical calculation results are described.

In Chapter 2, the configurations of the VHF sensor and the Maido-1 satellite in detail are described. The VHF sensor on Maido-1 satellite had conducted 158 lightning observations all over the world and proved its function in space. There seems to be regional difference of lightning flash rate. In previous studies, the OTD and LIS observed the distribution of lightning on the globe. The regional differences of lightning source positions are discussed. From the observations with the VHF sensor, it is also confirmed to be possible to observe lightning activities using radio wave from orbit [15].

In Chapter 3, the relationship between 116 VHF sensor events recorded by the VHF sensor on the Maido-1 satellite and lightning strokes detected by the WWLLN is discussed in order to show that most of the VHF sensor events were caused by lightning discharges. For each VHF sensor event, the WWLLN events within 1400 km from the subsatellite point and within 1 sec, 30 sec, and 300 sec of the VHF sensor trigger time are analyzed. In addition, for the 6 VHF sensor events, the arrival directions of EM waves are estimated using the propagation time delay differential at each frequency [16].

In Chapter 4, the discussion and new knowledge on the wave propagation characteristics in the ionosphere are discussed from the lightning observations with the VHF sensor. First, the change of the pulse width with the electromagnetic wave propagation in the ionosphere is discussed. The numerical calculation indicates that the full width at half maximum (FWHM) is changed by the incident angle to the ionosphere. The pulse

widths of the received pulses are compared with those of the numerical calculations [17]. Second, some waveforms recorded by the VHF sensor involved the pulse pairs with the time intervals about tens of nanoseconds. The cause of the pulse pairs is discussed. A numerical calculation to understand the cause of the pulse pairs is made for the characteristics of the radio propagation using the ionospheric model considering the altitude distribution of the electron density and the earth's magnetism. The arrival time differences between the electromagnetic ordinary (O) and extraordinary (X) modes are calculated. The satellite observation results are compared with the numerically calculation results of arrival time difference between the two modes.

In Chapter 5, the outline of global lightning and sprite measurements (GLIMS) mission is described. In order to study the generation mechanism of lightning associated transient luminous events (TLEs) and the relationship between lightning and TLEs, the lightning and TLE observation at Exposed Facility of Japanese Experiment Module (JEM-EF) of International Space Station (ISS) will be carried out [18]. In this mission, the arrival direction of the lightning radiation source using the VHF broadband digital interferometer (VITF) will be estimated [19]. The error of the estimated arrival direction of the lightning radiation source is calculated [20].

In Chapter 6, the results obtained by this investigation are summarized.

# Chapter 2

## VHF sensor on the Maido-1 satellite

### 2.1 Introduction

The broadband measurement for waveforms of VHF lightning impulses (VHF sensor) had developed for a research on lightning discharges. The aim of the sensor is to examine the feasibility of the space-borne VHF DITF, which is a system to locate sources of impulsive VHF radiation. In this chapter, the observations with the VHF sensor on the Maido-1 satellite are described. Section 2.2 describes basic concepts of Maido-1 satellite and the configurations of the Maido-1 satellite and VHF sensor. Section 2.3 shows the observation procedures. Section 2.4 presents the typical observation results and summarizes this chapter.

### 2.2 Maido-1 satellite and VHF sensor

#### 2.2.1 Basic concept

Maido-1 satellite project represents a technology transfer program to expand the range of the space development community in Japan. The aim of the project is to get small-and-medium-sized manufacturing enterprises (SMEs) involved in small space projects and new space technologies. Under the cooperative agreement, Japan Aerospace Exploration Agency (JAXA) intends to contribute to socio-economic development by returning its research and development (R&D) results to society and SOHLA (Space Oriented Higashiosaka Leading Association) tries to revitalize the local economy through the commercialization of versatile small satellites. According to the agreement, JAXA provides SOHLA their technical

information on small satellites and other technical assistance for the development of the small satellites, Maido-1. The prime objective of the Maido-1 satellite project is to realize low-cost and short term development of a microsatellite which utilizes the components and bus technologies of JAXA's MicroLabSat [21]. Maido-1 is a spin-stabilized microsatellite on MicroLabSat heritage with the weight of 56 kg. The spin axis is fixed to the inertial reference frame. The spin axis lies in the plane containing the solar direction and the normal to the orbital plane. LRG-OU takes responsibility for the main science mission of Maido-1 satellite.

### 2.2.2 Maido-1 satellite configuration

Maido-1 satellite was launched on 23 January 2009. It is in sun-synchronous polar orbit at an altitude of 660 kilometers. It goes round the earth 15 times a day. Figure 2.1 shows the illustration of the Maido-1 satellite. Table 2.1 shows the specification of the Maido-1 satellite.

The satellite carries the radio-frequency payload, which terms 'the VHF sensor', for research on lightning. The Maido-1 satellite is the world's first specialized satellite for lightning observation.



Fig 2.1 Illustration of the Maido-1 satellite

Table 2.1 Specification of the Maido-1 satellite

Size	470×470×400 mm
Weight	56 kg
Orbit	SSO
Altitude	660 km
Cycled Period	About 1.6 hours
Spin Rate	3-11 rpm

### 2.2.3 VHF sensor configuration

The VHF sensor is designed and developed by LRG-OU to receive VHF lightning impulses on the satellite orbit. Figure 2.2 shows the configuration diagram of the sensor. The sensor consists of a monopole antenna with the length of 1.0 m, a band-pass filter (BPF), an amplifier (AMP) and an analog-to-digital converter (ADC) to record broadband VHF signals. BPF, AMP and ADC are integrated in a box with DC/DC converter and transceiver unit as shown in Figure 2.3. Table 2.2 shows the specification of the sensor.

The electromagnetic (EM) waveforms with duration of 2.5  $\mu$ sec could be recorded by the level trigger system. Once the level of received signal exceeds the threshold, a waveform of 512 samples is stored in its memory, consisting of 128 samples preceding and 384 samples following the trigger. The maximum number of EM waveforms (the number of the trigger) for one event was 100 due to the size of the onboard memory of the AD converter. The trigger event is usually the input waveform data reaching some user-specified threshold voltage (trigger level) in the positive direction.

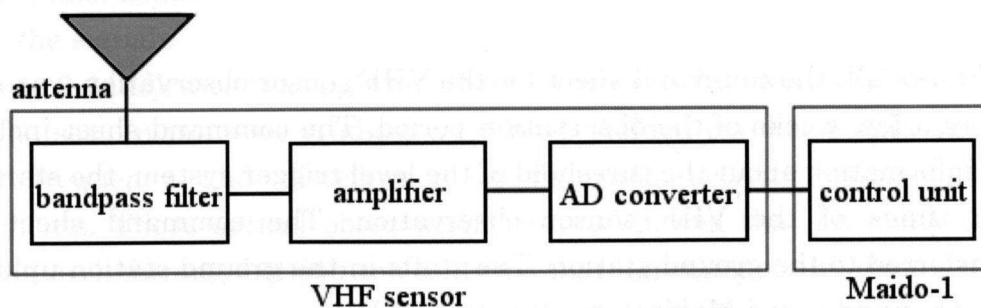


Fig 2.2 Diagram of the VHF sensor

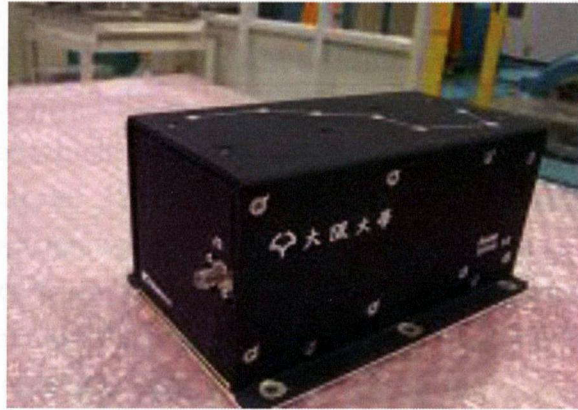


Fig 2.3 Overview of the VHF sensor

Table 2.2 Specification of the VHF sensor

Antenna type	Monopole (1.0 m)
Passband of BPF	30-100 MHz
Sample rate of ADC	200 MHz
Gain of AMP	45 dB
Size	100×80×150 mm
Wight	950 g
Power	4W (5 V : 1.8 W, 15 V : 2.2 W)

## 2.3 Observations

### 2.3.1 Procedures

First of all, the command sheet for the VHF sensor observation was made before a few weeks of the observation period. The command sheet included the information about the threshold of the level trigger system, the start and stop times of the VHF sensor observation. The command sheet was transferred to the ground station. The staffs in the ground station uploaded the command to the Maido-1 satellite (uplink).

The Maido-1 satellite receives the command, and then executes the VHF

sensor command at the specified time. The VHF sensor starts the lightning observation by the command. When the VHF sensor is activated, it records the number of the recorded EM waveforms in several seconds and time with accuracy of 1 second as the House Keeping (HK) data, even if the number of the recorded EM waveforms is 0. When the number of the recorded waveform data reaches 100 or the end time of the observation, the VHF sensor stops the observation. And then, the observation data were downloaded to the ground station (downlink). The downloaded data include the two observation data, the waveform data and the HK data.

### 2.3.2 Observation Period

The radio observations with the VHF sensor at night time from February 12 to October 7, 2009 are conducted. During the observation period, the VHF sensor was activated 158 times. The lightning observations had been particularly conducted in February, April and June, 2009. In October, the function of the VHF sensor had been checked whether it works well or not. The observation in October indicated the VHF sensor had maintained the normal functioning during the 8 months after the launch.

## 2.4 Observation results

Figure 2.4 shows the locations where the sensor was activated in the five months. Plus sign indicates the location detected VHF signals from the lightning discharges. Triangle shape indicates the location detected a few VHF signals. Diamond shape indicates the locations where the sensor didn't detect the signals

Figure 2.4 indicates that lightning activity is more frequent on shore than over the sea. In previous studies, OTD have yielded extensive data on the global frequency and distribution of lightning activity using optical equipments. These optical observation results showed that an analysis of this annual lightning distribution confirms that lightning occurs mainly over land areas, with an average land/ocean ratio of  $\sim 10:1$  [22]. The results using the VHF sensor on Mado-1 satellite agree with past investigations. Though

the sensor received the lightning signals above the Atlantic Ocean, these results mean that it received the propagated signals through the ocean from

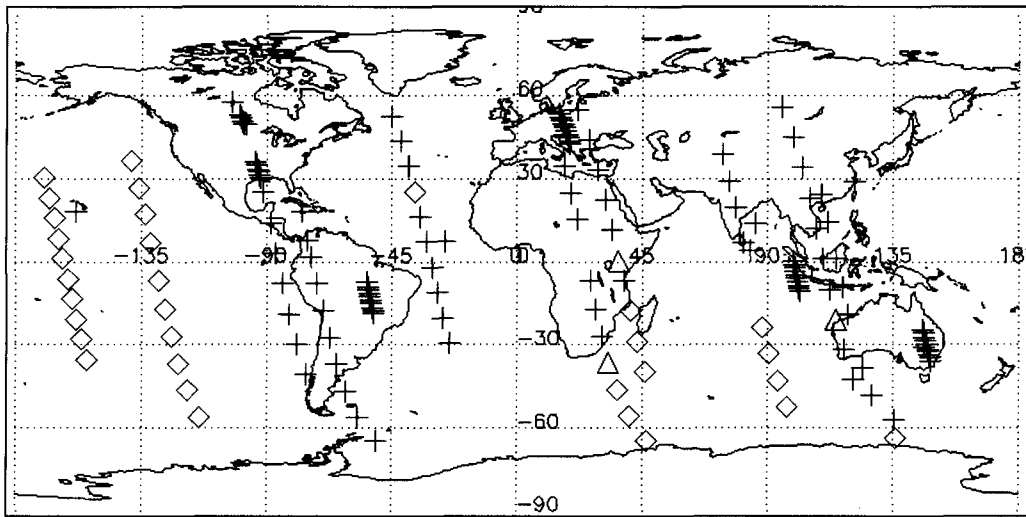


Fig 2.4 The locations of observed VHF signals

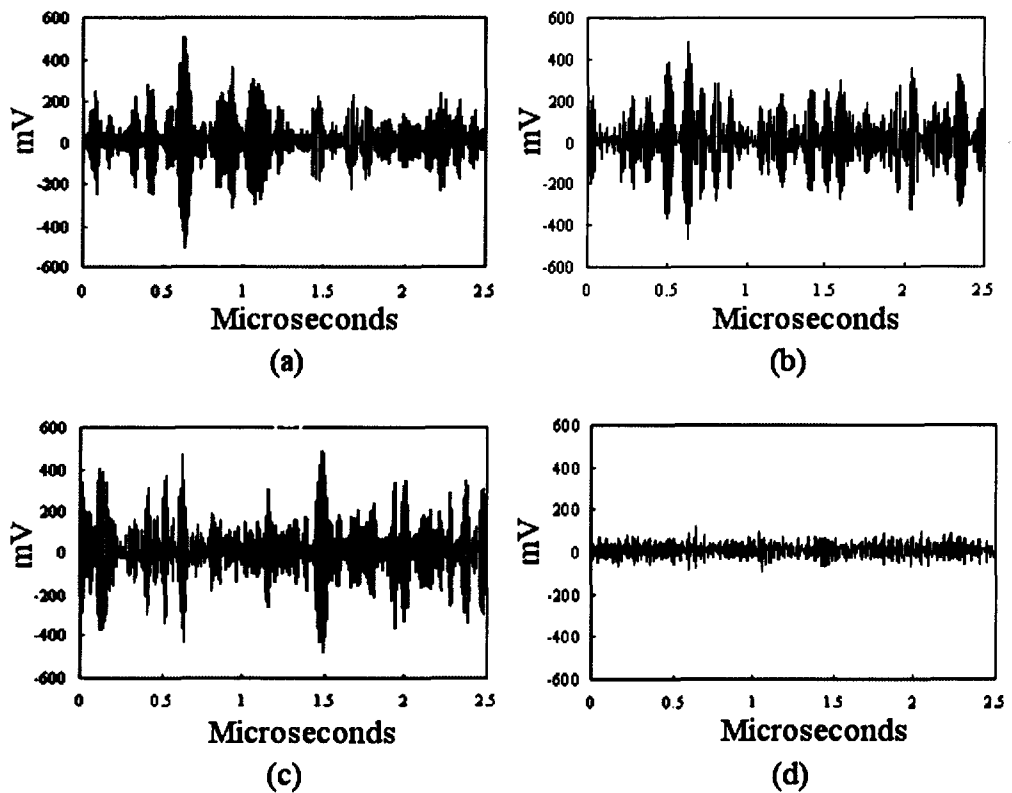


Fig 2.5 EM Waveforms recorded by VHF sensor

the radiation source near the African or the American continent.

Figure 2.5 shows the lightning signals detected at four different areas. Figure 2.5(a) shows the recorded EM waves by the sensor above eastern Australia. Figure 2.5(b) and 2.5(c) show observations above Southeast Asia and the Atlantic Ocean, respectively. Figure 2.5(d) shows the signal recorded above the Pacific Ocean where a non-lightning activity area. When the impulsive pulses propagate through the dispersibility medium, the pulse width broadens for a different propagation velocity of each frequency. The EM intensity in non-lightning area is very small. The results indicate that the lightning activity using radio waves is possible from the orbit. Also the results indicate that it is possible to observe the lightning activity using radio waves from orbit. The signals of various waveforms had been recorded above the world. The observed waveform shows regional dependence. This means that there are regional characteristics for waveform. The variation of waveforms is thought to be due to lightning activity factor and the propagation distance between the satellite and radiation source.

## 2.5 Conclusion

The VHF sensor on Mado-1 satellite was conducted 158 lightning observations around the world. The results indicate the frequency of the lightning activity was higher on shore than at sea. The possibility to observe lightning activities using radio wave from orbit has been confirmed. There are regional characteristics for waveform because the observed waveform of the lightning varied with observation area.



# Chapter 3

## Evaluation of VHF sensor observations

### 3.1 Introduction

In this chapter, the evaluation of the radio observations using the VHF sensor is presented. To evaluate the Mado-1 satellite observation results, we use the World Wide Lightning Location Network (WWLLN) data. Many ground based lightning observation systems are installed all over the world such as National Lightning Detection Network in North America [6], Brazil Integrated Network [23], New Zealand Lightning Detection Network [24], and Canadian Lightning Detection Network [25]. These lightning location systems cannot observe the lightning activities all over the world using each system, while the observational area of the WWLLN is almost all areas of the world. The WWLLN is a real-time and world-wide ground network that detects preferentially strong lightning strokes [26]. The relationship between the VHF electromagnetic (EM) waves recorded by the VHF sensor and lightning strokes located by the WWLLN is discussed and careful analyses of 6 coincident events for estimating the arrival direction of the recorded VHF EM waves are performed.

Section 3.2 shows a datasets of the VHF sensor and the WWLLN. Section 3.3 presents a methodology to compare the VHF sensor event to the WWLLN event. Section 3.4 describes the comparison results. Section 3.5 also summarizes this chapter.

## 3.2 Datasets

### 3.2.1 VHF sensor

During the observation period, the VHF sensor was activated 158 times. In 158 activations, 116 data were successfully downloaded to the ground station. The other 42 data were not completely downloaded due to the satellite communication error.

In this thesis, the 116 successfully downloaded data are termed here 'VHF sensor events'. Among the 116 VHF sensor events, the numbers of EM waveforms were 100 and 65, respectively, in the 98 events and only one event. In the other 17 VHF sensor events, very few EM waveforms were recorded. In the 99 VHF sensor events, 100 EM waveforms of 7 VHF sensor events were downloaded to the ground station.

### 3.2.2 World Wide Lightning Location Network

The WWLLN is a real-time and world-wide ground network that detects preferentially strong lightning strokes. The WWLLN receivers detect the very low frequency (VLF; 3-30 kHz) radiation from a lightning stroke and use the time of group arrival (TOGA) at least 5 stations to locate the position

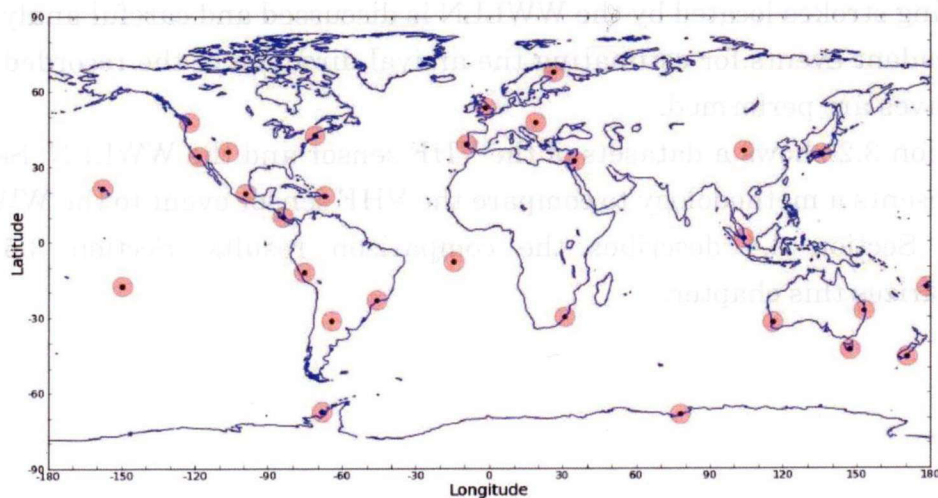


Fig. 3.1 Locations of the WWLLN sensors in 2009 [25].

of the lightning. The propagation and low attenuation of VLF waves in the Earth-Ionosphere waveguide allow a global and real-time detection of lightning activity with fewer antennas compared with other ground detection systems [23], [26], [27], [28], [29]. The estimated efficiency of the WWLLN was 30-35 % for discharges with peak current  $> 50$  kA and about 10 % overall [30]. The WWLLN had an average RMS timing accuracy of  $30 \mu\text{s}$  and was localized to about 20 km. Figure 3.1 shows the Locations of the WWLLN sensors in 2009 [25].

### 3.3 Methodology

#### 3.3.1 Coincidence rate

Figure 3.2 shows the 99 subsatellite points where the VHF sensor events were detected, as shown the square shape, and the 4 analyzed areas. Afterward we focus on the 4 areas as shown in Fig. 3.2. Areas 1 (A1), 2 (A2), 3 (A3), and 4 (A4) are the North and South American continents, the African and European continents, Southeast/East Asia and the Australian continent, and the Pacific and Atlantic Oceans. Furthermore, the 17 VHF sensor events

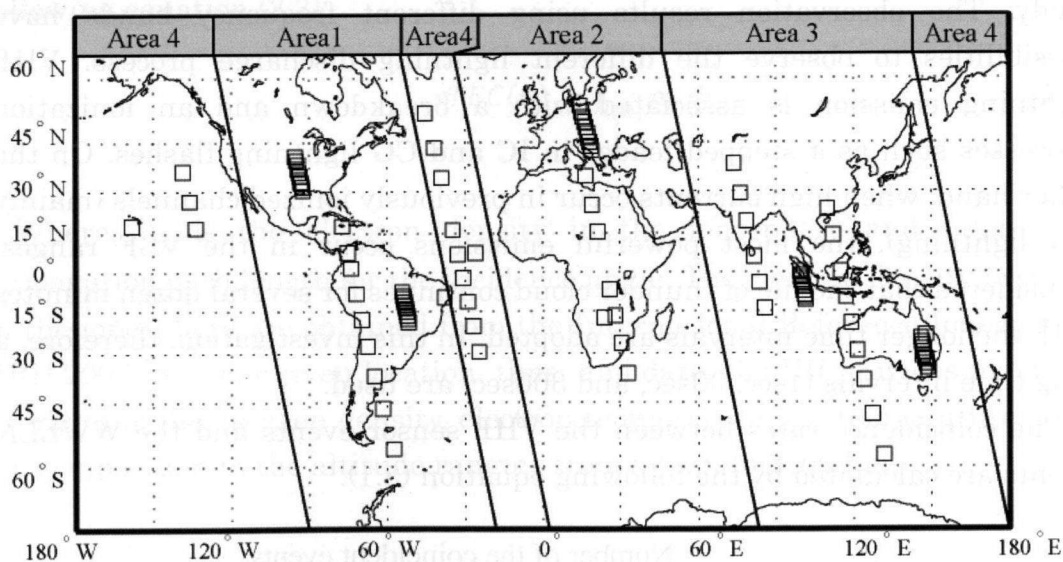


Fig. 3.2 The subsatellite points of the 99 VHF sensor events and the analyzed areas. The square shape shows the subsatellite point of the VHF sensor event.

recorded very few EM waveforms are analyzed as Undetectable Events (UEs).

The Mado-1 satellite's altitude determines its geometric FOV, which extends to about  $64^\circ$  of the nadir angle corresponding to a distance of 2000 km from the subsatellite point at ground level. Considering the radiation pattern of the monopole antenna, which exhibits typical figure of eight pattern in the E-plane, VHF EM waves radiated by lightning discharges close to the horizon are effectively undetectable. Consequently, a somewhat smaller effective FOV is assumed to extend out to only  $60^\circ$  of the nadir angle, which corresponds to a distance of 1400 km from the subsatellite point.

To find the events detected by both VHF sensor and WWLLN coincidentally, first, any WWLLN events that are more than 1400 km away from the subsatellite point are excluded. From this reduced WWLLN data set, the WWLLN spheric time is compared with the VHF sensor trigger time. In case one or more WWLLN events are detected within 1 sec, 30 sec, and 300 sec of the VHF sensor trigger time, the event is defined as the coincident event.

Many investigations have been reported that a short time interval within 0.1 sec is normally used in the comparison research between the different lightning detectors [23], [24], [25], [26].

The lightning events detected by two different frequency band, (namely) VHF and VLF bands with VHF sensor and WWLLN, are compared in this study. The observation results using different frequency bands have possibilities to observe the different lightning discharge process. VHF lightning emission is associated with a breakdown and an ionization processes such as a stepped leader in IC and CG lightning flashes. On the other hand, when high currents occur in previously ionized channels (mainly CG lightning), the most powerful emissions occur in the VLF ranges. Considered that the life of thunder cloud continues for several dozen minutes [31], the longer time intervals are adopted. In this investigation, therefore, a long time intervals (1sec, 30sec, and 300sec) are used.

The coincidence rates between the VHF sensor events and the WWLLN events are calculated by the following equation (3.1).

$$\text{Coincidence rate} = \frac{\text{Number of the coincident events}}{\text{Total number of the VHF sensor events}} \quad (3.1)$$

### 3.3.2 Estimation of arrival direction of EM waves

Next, the EM waveforms of the downloaded events are discussed to indicate the relationship of the radiation source locations of lightning discharges. The Earth's ionosphere introduces group delay, the Faraday rotation, and refraction effects to EM waves propagating through this medium. The propagation time delay differential at each frequency is used to estimate the arrival directions of EM waves. In order to obtain the propagation delay of the recorded EM waves, the spectrogram of the EM waveform is calculated by the Short Term Fourier Transform (STFT) with a Gaussian window of a length of 0.64  $\mu$ s. The VHF propagation time delay due to the total electron content (TEC) along a path is given by the following equation (3.2) [32].

$$\Delta t = \frac{1.34 \times 10^{-7}}{f^2} \times sTEC(\theta) \quad (3.2)$$

Where,  $\Delta t$  is the propagation time delay in second,  $f$  is the radio frequency in Hz, and  $sTEC(\theta)$  is the slant TEC on the propagation path for the incidence angle  $(\theta)$ . The incidence angle is defined as the angle between the arrival directions of EM waves and the nadir direction of the satellite.  $sTEC(\theta)$  is the following equation (3.3).

$$sTEC(\theta) = \int_{l(\theta)} n_e ds. \quad (3.3)$$

Where,  $n_e$  is the electron density in the ionosphere and  $l(\theta)$  is the propagation path length for the incidence angle. The electron density profiles in the ionosphere are obtained from the International Reference Ionosphere (IRI) 2007 [33]. For given location, time, and date, the IRI provides monthly averages of the electron density, electron temperature, ion temperature, and ion composition in the altitude ranging from 50 km to 2000 km.

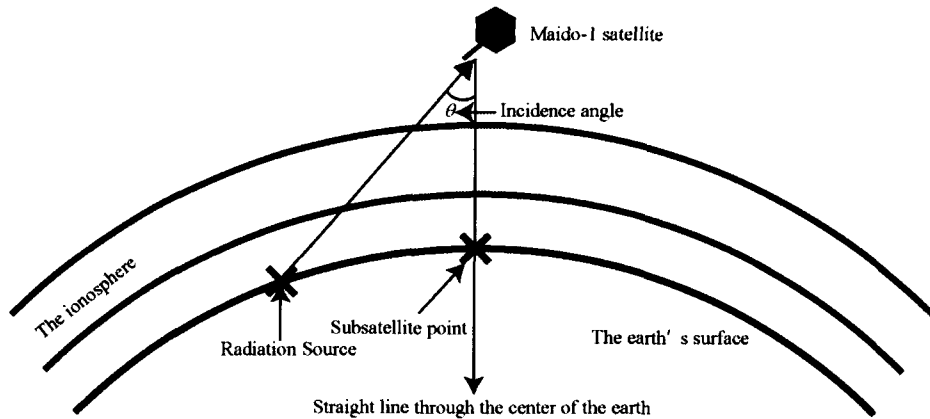


Fig. 3.3 The simple ionosphere model (not to scale)

The simple ionosphere model is used to estimate the incidence angle of EM waves as shown in Fig. 3.3. In this model, the radius of the Earth is 6370 km and the lowest altitude of the ionosphere is a height of 80 km. In a very general sense, for the VHF propagation characteristics in the nighttime ionosphere, the effect of the wave refraction under moderate ionospheric conditions is ignored. The IRI provides the data set of the electron density every 10 km in the ionosphere and the vertical TEC above the subsatellite point. It is assumed that the altitude distribution of the electron density along the propagation path is the same distribution along the nadir direction and the slant TEC in each incidence angle is determined. The theoretical curve of the propagation time delay is calculated by equation (3.2).

The following procedures are conducted to estimate the incidence angle for one EM waveform recorded by the VHF sensor.

1. We find the maximum values of the spectrogram at each frequency.
2. We set the threshold value as the 0.8 times maximum value at each frequency.
3. We find the maximum value in the time interval of  $0.64 \mu\text{s}$  moving along the time axis by a  $5 \text{ ns}$  step. The maximum value over the threshold value in the time interval was determined in every step.
4. The theoretical curve is calculated by Eq. (3.2) in an incidence angle.
5. Compared between the maximum values and the theoretical curve, a fitted curve is calculated by the least squares method.

6. Repeating the steps 4 and 5 for the theoretical curve in all incident angles from 0 to 60 degree, the most likelihood incidence angle (the estimated incidence angle) is calculated.

The most likelihood curve and the estimated incidence angle for every EM waveform are determined.

## 3.4 Results and discussion

### 3.4.1 Coincidence rate

Table 3.1 shows the coincidence rates between the VHF sensor events and the WWLLN events in 4 areas and for the UEs. The first column shows the areas and the UEs.

The second column shows a total number of the VHF sensor events. The third, fourth, and fifth columns show the coincidence rates between the VHF sensor events and the WWLLN events within 1 sec, 30 sec and 300 sec, respectively, of the VHF sensor trigger time. In the fifth column of Table 3.1, in particular, the coincidence rates in A1 and A3 are greater than 0.90. On the other hand, the coincidence rates in A2 and A4 are less than 0.61. The coincidence rate for the UEs is 0.04.

The coincidence rate for the UEs, which is 0.04, indicates that there was almost no lightning activity in the area where the VHF sensor detected very few EM waveforms. The result suggests that the VHF sensor events are not

Table 3.1 The coincidence rates between the VHF sensor events and the WWLLN events within 1 sec, 30 sec and 300 sec, respectively, of the VHF sensor trigger time in the 4 areas and for the UEs

Area	Total number of VHF sensor events	Coincidence Rate		
		$\leq 1$ sec	$\leq 30$ sec	$\leq 300$ sec
A1	30	0.17	0.50	0.90
A2	18	0.06	0.28	0.61
A3	37	0.05	0.78	0.95
A4	14	0.00	0.07	0.21
UEs	17	0.00	0.00	0.04

the artificial noise from the satellite or the earth. If the VHF sensor event which was detected as a signal depends on the noise such as artificial noise from the satellite or the earth, the undetectable event is hardly possible to observe. The high coincidence rates in A1 (the North and South American continents) and A3 (Southeast/East Asia and the Australian continent) indicate that the VHF sensor events have a good agreement with the WWLLN events. On the other hand, the coincidence rates in A2 (the African and European continents) and A4 (the Pacific and Atlantic Oceans) are smaller than in the other areas. It is speculated that the reason why the small coincidence rates in A2 and A4 is the regional differences of the detection efficiencies of the WWLLN.

According to the previous study [26], the detection efficiency in Africa is smaller than that elsewhere because the WWLLN station density in Africa was rather low. It seems that the coincidence rate in A2 (the African and European continents) is smaller than expected because of the low detection efficiency of the WWLLN in Africa. From the comparison of the PDD on the FORTE satellite and the WWLLN, the small percentage difference in land versus ocean coincidence detection efficiency indicates that it is unlikely that the WWLLN will completely miss a storm with lightning of similar magnitude over ocean relative to over land [34].

The coincidence rate in A4 seems to disagree about the previous study, but the detection efficiency of the WWLLN over all areas of oceans is not completely understood. It is believed that, because the detection efficiency of the WWLLN depends on the number of the stations around the radiation sources, the detection efficiency decreases for the radiation sources about a few Mm away from the station like a central of the Pacific and Atlantic Oceans.

### 3.4.2 Estimation of arrival direction of EM waves

Next the relationship between the EM waveforms of the VHF sensor event and the location of WWLLN lightning strokes is discussed. The 100 EM waveforms were downloaded at the 7 events of the 116 VHF sensor events. There are the 6 coincident events that have the full waveforms.

Table 3.2 shows the 6 coincident events and the number of the WWLLN events that meet the criteria for each coincident event. The first column shows the date and time of the VHF sensor trigger time. The second and third columns show the latitude and the longitude of the subsatellite point, respectively. The fourth column shows the number of the downloaded EM waveforms. The fifth, sixth, and seventh columns show the number of the WWLLN events that meet the criteria for each coincident event within 1 sec, 30 sec and 300 sec, respectively, of the VHF sensor trigger time for those events. For the 6 coincident events, the incidence angles of EM waves using the methodology shown in Section 3.3 are estimated.

Fig. 3.4 shows the typical spectrogram and the arrival direction estimation for the VHF sensor event. The circle and line indicate the most likelihood curve. The double-headed arrows are the frequency bandwidth employed for arrival direction estimation or considered to be the artificial noise. The triangle signs are the maximum values at each frequency. The most appropriate frequency bandwidths are employed to estimate arrival direction for each event. When the spectrogram constantly contains the high intensity at certain frequencies, the frequencies are not used in this thesis. The time-frequency analysis in Fig. 3.4 seems to indicate the observation results

Table 3.2 The 6 coincident events and the number of the WWLLN events that meet the criteria

Date & Time (mmddhhmmss)	Latitude (deg)	Longitude (deg)	Number of DL waveforms	Number of WWLLN events		
				≤ 1 sec	≤ 30 sec	≤ 300 sec
0212151129	-23.65	147.80	100	0	1	4
0212232329	-17.38	23.83	100	1	1	15
0224181306	4.02	98.31	100	0	2	13
0225151956	-24.84	145.89	100	0	4	31
0609230705	-6.73	26.06	100	0	1	44
0610022705	7.51	-25.94	100	0	4	86

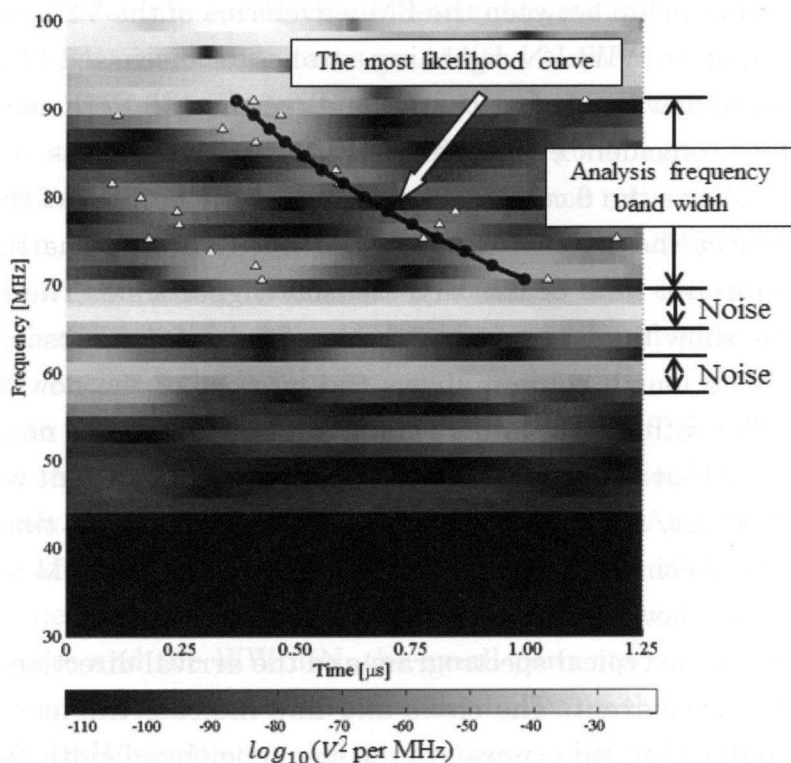


Fig. 3.4 The typical spectrogram and the directions of arrival estimation for the VHF sensor events. The circle and line indicate the most likelihood curve. The double-headed arrows are the frequency bandwidth employed for arrival direction estimation or considered to be the artificial noise. The triangle signs are the maximum values at each frequency.

of receiving the artificial radio waves. In this thesis, when the spectrogram constantly contains the high intensity at certain frequencies, the frequencies are not used. We thought that the frequencies are the artificial radio waves from the ground facilities such as a radio station. The artificial radio waves from the ground facilities, however, have narrowband (a few MHz) width compared to our analysis frequency band width (30-100MHz). It is believed that the artificial radio waves have relatively little effect on our studies. The low frequency bandwidth, which is less than 65 MHz, is not used since the dispersion characteristics of EM waveforms are often obscured.

For all the downloaded EM waveforms of the 6 events, which is a total of 600 EM waveforms, the incidence angles using the above methodology are estimated. The estimated incidence angles for the VHF sensor events are compared with those for the WWLLN events that meet the criteria, as shown in Fig. 3.5.

The box plot, as shown in (i), indicates the distribution of the estimated incidence angles for all the downloaded EM waveforms. The central line between the two boxes corresponds to the median of all the estimated incidence angles, and the lower and upper edges of these boxes correspond to the 25 and 75 percentiles (Q1, Q3). The whiskers correspond to the lowest datum still within 1.5 interquartile range ( $IQR = Q3 - Q1$ ) of the lower quartile, and the highest datum still within 1.5 IQR of the upper quartile. The outliers are plotted individually by plus sign.

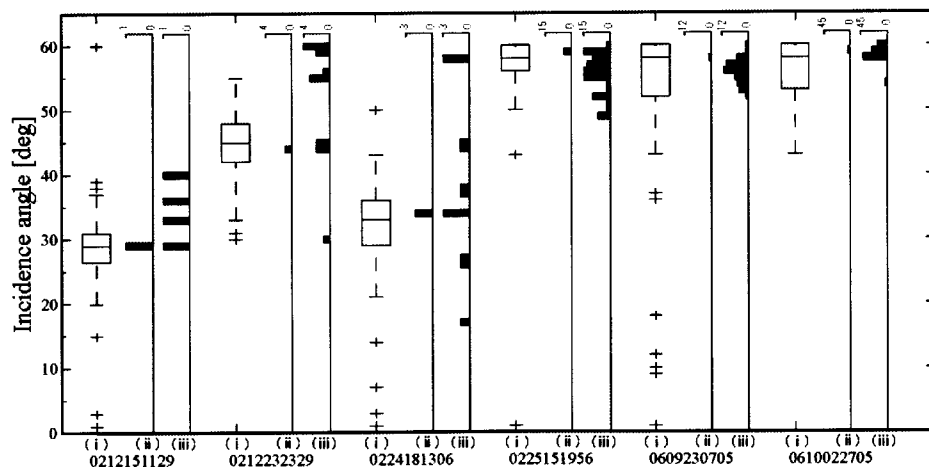


Fig. 3.5 The comparison between the estimated incidence angles for the VHF sensor events and those for the WWLLN events that meet the criteria for all the 6 VHF sensor events. The box plot, as shown in (i), indicates the distribution of the estimated incidence angles for all the downloaded EM waveforms. The histograms, as shown in (ii) and (iii), are the distributions of the estimated incidence angles for the WWLLN events that occurred within 30 sec and 300 sec, respectively, of the VHF sensor trigger time

The histograms, as shown in (ii) and (iii), are the distributions of the estimated incidence angles for the WWLLN events, which are shown in the sixth and seventh columns of Table 3.2, within 30 sec and 300 sec, respectively, of the VHF sensor trigger time.

In Fig. 3.5, compared the median of the estimated incidence angles for the VHF sensor events with those for the WWLLN events within 30 sec of the VHF sensor trigger time, the difference is within 1 degree for each event. The temporal and spatial coincidences show a clear relationship between the VHF sensor events and the lightning discharges located by the WWLLN. These results indicate that the both sensors detected the EM events of lightning discharges produced by the same thunderstorm or thunderstorms which are close to each other. Compared with the distributions of the WWLLN events within 300 sec of the VHF sensor trigger time, the estimated incidence angles are roughly in accordance with the distribution for all the VHF sensor events. Most of the recorded EM waves seem to be associated with the WWLLN events within 30 sec of the VHF sensor trigger time. Some outliers imply that the VHF sensor recorded the EM waves in various directions. A few outliers, however, seem to include obviously incorrect angles.

The WWLLN using VLF band is the most efficient at detecting return strokes of CG lightning but is also sensitive to some IC lightning. On the other hand, the VHF sensor is thought to receive the EM waves radiated from lightning discharge process such as stepped leader, return stroke and narrow bipolar event [4] [35], [36]. According to the difference of the observed frequency bands, it is noteworthy that the estimated incidence angles for the VHF sensor events are in good agreement with those for WWLLN events.

### 3.5 Conclusion

The relationship between VHF EM waves detected by the VHF sensor on the Mado-1 satellite and lightning discharges is described. All 116 VHF sensor events were compared to the WWLLN events. It is found that the coincidence rates in the North and South American continents, and in Southeast/East Asia and the Australian continent are greater than 0.90. The VHF sensor events had a good agreement with the WWLLN events in these areas. On the other hand, the coincidence rates in the African and European continents, and in the Pacific and Atlantic Oceans were less than 0.61. We speculate that the regional difference of the detection efficiency of the WWLLN caused the difference in the coincidence rates in the 4 areas. In addition, we focused on the 6 coincident VHF sensor events that have 100 EM waveforms. The incidence angles of EM waves for VHF sensor were estimated. Compared the median of the estimated incidence angles for the VHF sensor events with those for WWLLN events within 30 sec of the VHF sensor trigger time, the difference was within 1 degree. The temporal and spatial coincidences showed a clear relationship between the VHF sensor events and the lightning discharges located by the WWLLN. These results indicated that a large fraction of the VHF sensor events are coincident with lightning discharges.



# Chapter 4

## Analysis of VHF electromagnetic waveforms in the ionosphere

### 4.1 Introduction

In this chapter, the propagation characteristics of the broadband electromagnetic waves radiated from lightning are discussed. Section 4.2 describes the change of the pulse width of electromagnetic waves through the ionosphere using the numerical calculation. The pulse widths of the observed electromagnetic waves above the Atlantic Ocean area and Southeast Asia area are compared with the numerical simulation results. Section 4.3 presents the observed waveforms included the pulse pairs with the time intervals about tens of nanoseconds, and the cause of the pulse pairs from a comparison between numerical calculations and observation results is discussed.

### 4.2 Change of the pulse width

#### 4.2.1 Numerical study

When the electromagnetic wave propagates through the dispersive medium such as the ionosphere, the waveform is affected by the group delay. The pulse width grows wider in the medium because the short duration VHF pulse with lightning activity has the wide band frequency characteristic. The numerical simulation of the wave propagation was conducted in order to understand the change of the waveform using the ionospheric model as shown in Fig. 4.1.

The ionospheric model to calculate the characteristics of the radio propagation is used as shown in Chapter 3. The ionosphere is divided into multi-layers with the thickness of 10 km. The ionospheric model is grouped into 58-layers structure considering the altitude from 80 km to 660 km. Figure 4.1 shows the vertical structure of the ionosphere. Where  $O$  indicates the center of the earth,  $\theta_0$  is the initial incidence angle,  $\theta_i$  is the incidence angle to the  $i$ -th layer ( $i=1-58$ ) surface,  $R_0$  is the distance from the center of the earth to the bottom layer and  $R_i$  is the distance from the center of the earth to the  $i$ -th layer. The radius of the earth is assumed to be 6370 km. The value of the electron density in each layer is obtained from the international reference ionosphere 2007 (IRI-2007) model.

It is assumed that the electron density is constant in each layer. The refractive index in the ionosphere is calculated by the following equation (4.1).

$$n^2 = 1 - \frac{2X}{2(1-jZ) - \frac{Y^2 \sin^2 \phi}{1-X-jZ} \pm \sqrt{\frac{Y^4 \sin^4 \phi}{(1-X-jZ)^2} + 4Y^2 \cos^2 \phi}} \quad (4.1)$$

$$X = f_p^2 / f^2 \quad Y = f_c / f \quad Z = v_c / \omega$$

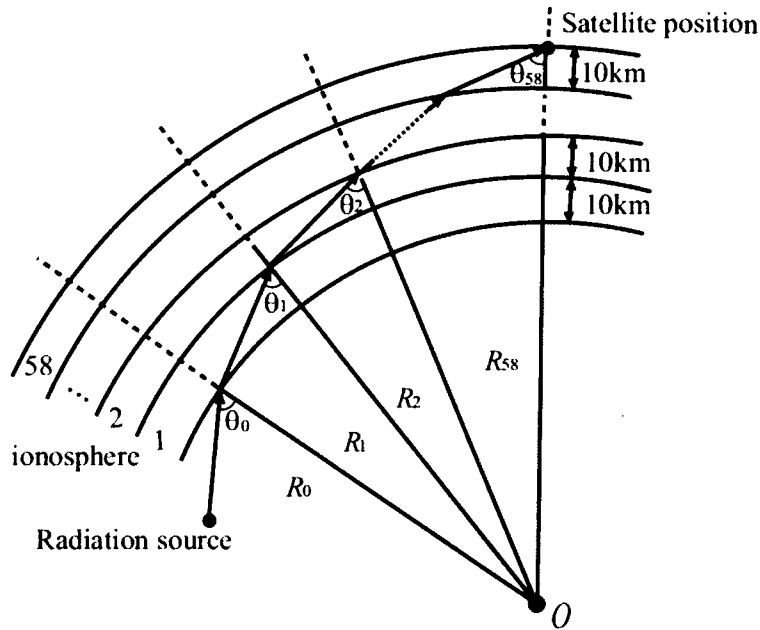


Fig. 4.1 The ionospheric model

Where,  $n$  is the refractive index,  $f$  is the radio frequency,  $f_p$  is the plasma frequency,  $f_c$  is the cyclotron frequency,  $\theta$  is the angle between the wave vector and the background magnetic field, and  $\nu_c$  is the collision frequency. When the electromagnetic wave propagates through the ionosphere, the left circular component travels as ordinary or O mode, while the right circular component travels as extraordinary, or X mode. The plus and minus signs in the equation (4.1) correspond to O and X modes respectively. The equation is called the Appleton-Hartree formula [38].

The plasma frequency is also calculated by the electron density as the following equation (4.2).

$$f_p = \left( \frac{n_e^2}{m\epsilon_0} \right)^{1/2} / 2\pi = 9.0\sqrt{n_e} \quad (4.2)$$

Where,  $m$  is the mass of the electron,  $n_e$  is the free electron density in the plasma and  $\epsilon_0$  is the permittivity of free space.

The cyclotron frequencies  $f_c$  are given by the following equations (4.3).

$$f_c = \frac{|e|B}{2\pi m} \quad (4.3)$$

Where  $e$  is the elementary charge and  $B$  is the background magnetic field (the earth's magnetism).

When  $f \gg f_c$ ,  $f \gg \nu_c$  and the equation does not consider the earth's magnetism, we can simplify the equation (4.1) as follows equation (4.4).

$$n = \sqrt{1 - \frac{f_p^2}{f^2}} \quad (4.4)$$

This equation to calculate the refractive index in the each layer is used. The propagation path in the ionosphere is calculated using the ray tracing method.

The following three factors are considered to make the incident waveform.

1. The band-pass filter of the VHF sensor has a pass bandwidth from 30 MHz to 100 MHz.

2. The spectrum of an event occurring within the clouds tends to peak near 60 MHz [5].
3. Intra-cloud discharges have greater mean power than that for cloud-to-ground discharges from the results of the satellite observation [12].

The incidence wave is constructed in consideration of the VHF wideband electromagnetic wave emitted from the lightning activities. The modulated Gaussian pulse by sine wave is used [39].

The incidence wave  $p(t)$  is given by the following equation (4.5).

$$p(t) = \begin{cases} e^{-\alpha(t-\tau_0)^2} \cos(\omega_t(t-\tau_0)) & (0 \leq t \leq \tau_0) \\ 0 & (\text{otherwise}) \end{cases} \quad (4.5)$$

Where  $\tau_0 = 5.0 \times 10^{-8}$  [s] ,  $\alpha = (2/\tau_0)^2$  and  $\omega_t = 11\pi/2 \tau_0$  [Hz] .  $\omega_t$  indicates the center frequency of the wave. Figure 4.2 shows the incidence wave. The duration time of the pulse is 100ns. The frequency bandwidth is from 30 MHz to 80 MHz. The full width at half maximum (FWHM) is 40 ns. The numerical calculation is done using the value of the electron density at  $0.30^\circ$  N,  $98.0^\circ$  E at 18:13:05 UTC on February 24, 2009.

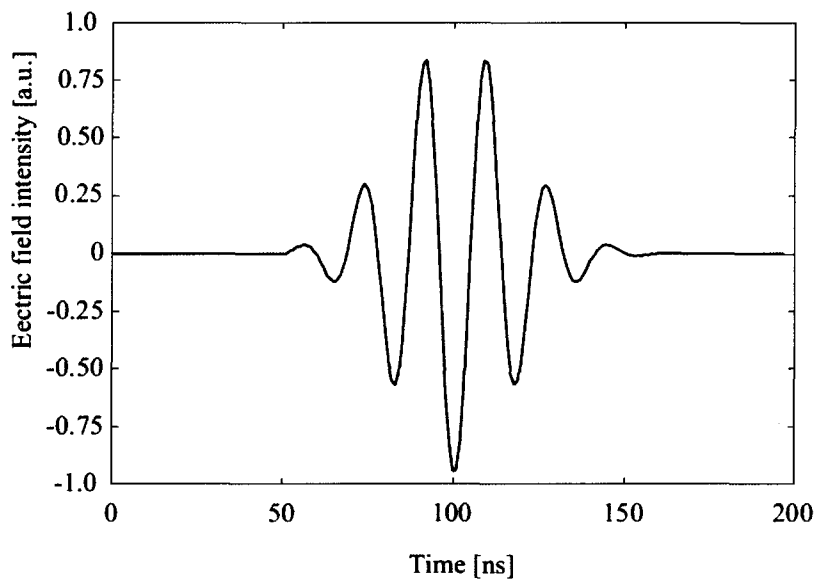


Fig. 4.2 Incident EM waveform emitted from lightning discharge in the numerical simulation.

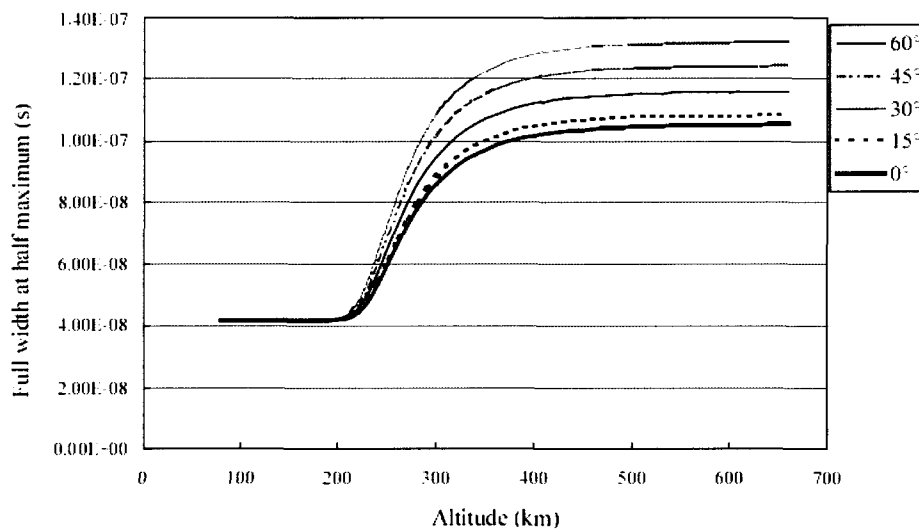


Fig. 4.3 The change of the FWHM from the bottom ionospheric layer (at 80 km altitude) to the satellite altitude layer (at 660 km)

Figure 4.3 shows the change of the FWHM from the bottom the ionospheric layer (at 80 km altitude) to the satellite altitude layer (at 660 km). The FWHM grows wider especially in the F-layer. The F-layer is the highest significant layer (at a height of around 200-400 km) in the ionosphere and the central part has the greatest electron density in the earth's atmosphere.

The incidence angle is defined as the angle between the incidence direction and the vertical direction to the bottom layer. When the incidence angle is  $0^\circ$ , the FWHM is about 100 ns. When the incidence angle is  $60^\circ$ , the FWHM is about 130 ns. The FWHM is changed by the incidence angle and increases to tens of nanoseconds as shown in Fig. 4.3. In other words, the FWHM depends on the distance between the radiation source and the observation point.

#### 4.2.2 Discussion about the pulse width

In this section, the pulse width of the observed pulses is discussed. The pulse width is calculated as follows.

The analytic signal of the observed pulse is calculated using the Hilbert transform. The envelope of the observed pulse is given by the absolute value of the analytic signal. We fit a logistic function to the envelope of the observed waveform. The logistic function is the following equation (4.6).

$$f(x) = \frac{1}{\sqrt{2\pi}\sigma x} e^{-(\ln x - \mu)/2\sigma^2} \quad (4.6)$$

We set the initial value for  $\sigma$  and  $\mu$ . When the error between the function and the envelope is a minimum value, an approximate envelope curve is defined. The FWHM of the observed pulses using the envelope curve is obtained.

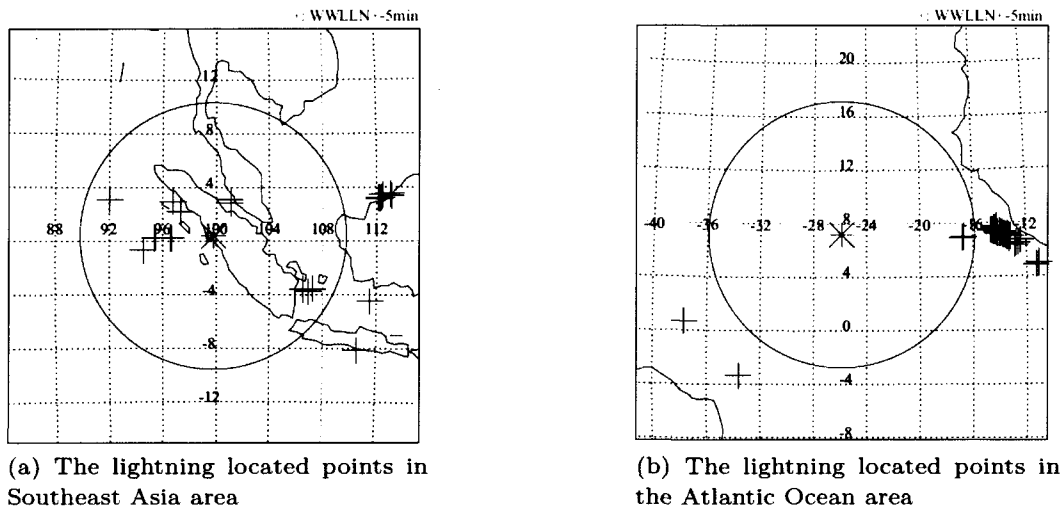


Fig. 4.4 The lightning located point by the WWLLN for 10 minutes (5 minutes before and after the satellite observation time)

In order to discuss the relationship between the pulse width and the incidence angle, the observation datasets are compared in two different areas. The VHF sensor recorded the datasets above Southeast Asia area and the Atlantic Ocean area. In this study, the location data obtained from the observational results by the WWLLN are used as the positions of the radiation source as is the case in Chapter 3.

Figure 4.4 shows the lightning location data with the WWLLN [25]. The center of the circle shows the location of the satellite at the time of satellite observation. The circle shows the satellite observational area and the radius is the observation range of VHF sensor. The pulse signs indicate the lightning location data by the WWLLN.

The detection efficiency of global lightning by the WWLLN is about several tens of percent. Although the satellite observation results cannot be compared directly with the results with WWLLN, the location of the thunderstorms with lightning activities using the location data is obtained by WWLLN. In general, the duration time of the thundercloud is several tens of minutes. Therefore it is reasonable that the WWLLN data for 600 seconds (300 seconds before and after the satellite observation time) as the position of the radiation source are used. In Fig. 4.4 (a), there are the lightning activities at the nearby satellite observation site in the Southeast Asia. On the other hand, the lightning activities are away from the satellite observation site in the Atlantic Ocean in Fig. 4.4 (b).

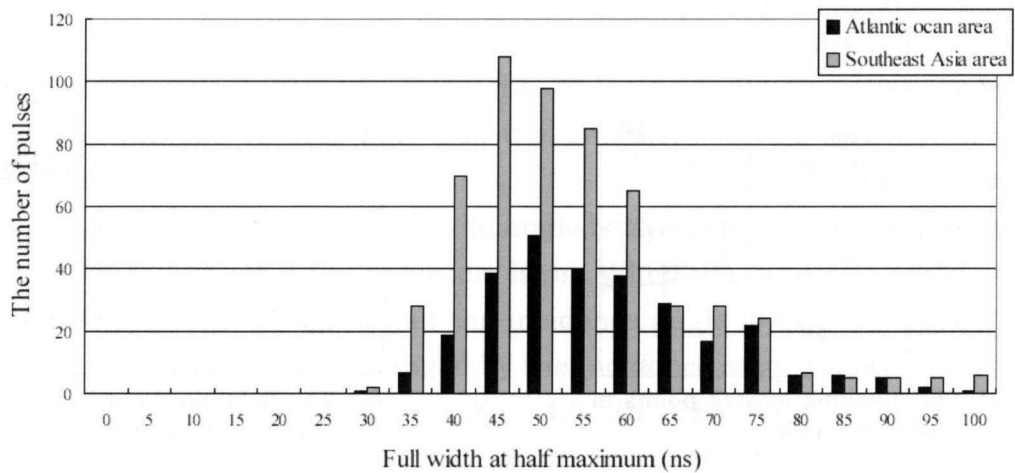


Fig. 4.5 The comparison of the pulse width observed in the two areas

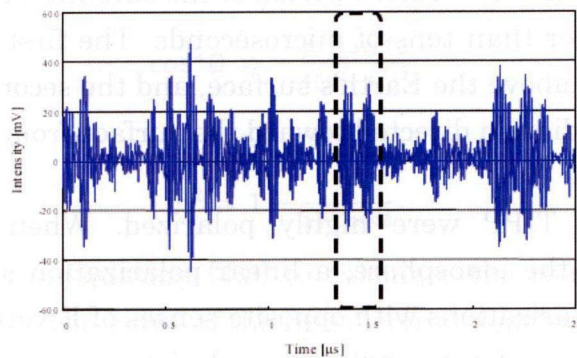
Figure 4.5 shows the comparison of the FWHMs of the received pulses in the two observation areas. The results in the Atlantic Ocean area have the greater FWHM than those in Southeast Asia area. The difference of the FWHM is about 5 ns. On the other hand, the results of WWLLN (in Fig.4.4) shows that the distance between the position of the radiation source and the observation site in the Atlantic Ocean area is longer than in South East Asia area. Our numerical calculation indicates that there is a close relationship between the FWHM and the propagation distance. When the FWHM is wider, the propagation distance is longer. The calculation results can explain two observational results (the VHF sensor and the WWLLN) qualitatively, even though the value of FWHM obtained by the numerical calculation is larger than the observation value.

These results are summarized as follows. From the comparison of the observed pulse widths by VHF sensor, it is found that the FWHM in the Atlantic Ocean area is greater than those in Southeast Asia. The difference of the FWHM is about 5 ns. On the other hand, from the results of the WWLLN, the distance between the radiation source and the observation site in the Atlantic Ocean area is longer than in Southeast Asia area. The calculation results are coincident to the observational results by the VHF sensor and the WWLLN.

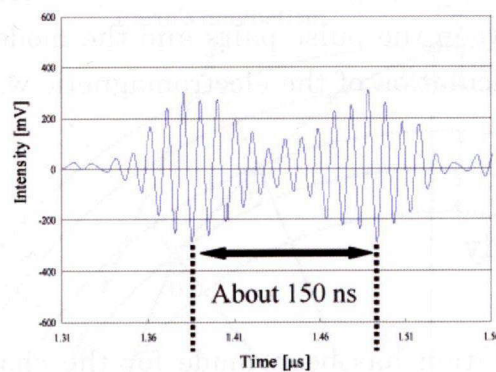
### 4.3 Pulse pairs recorded by VHF sensor

#### 4.3.1 Characteristics of the pulse pairs

As described above, Maido-1 satellite had conducted the observations all over the world. The VHF sensor received the several waveforms which included the pulse pairs above Southeast Asia and Central Africa. The two pulses making up the pulse pair had a similar amplitude and duration time.



(a) Example of observed pulse pair by Maido-1



(b) Extended figure of (a)

Fig. 4.6 Example of the observed pulse pair by Maido-1 above Southeast Asia area (Lat. 99.08°E, Lon. 0.30°N) at 18:13:06 UTC, February 24, 2009

The intervals of time between the peaks of the two pulses are from tens of nanoseconds to hundreds of nanoseconds. The pulse pairs appear in 20 waveforms among 100 waveforms which observed above Southeast Asia at 18:13:06 UTC, February 24, 2009 and in 10 waveforms among 100 waveforms above Central Africa at 02:27:05 UTC, June 10, 2009. Figure 4.6 (a) shows the example of observed pulse pair by the VHF sensor. Figure 4.6 (b) indicates the extended figure of Fig. 4.6 (a) from  $1.31\mu\text{s}$  to  $1.56\mu\text{s}$ .

In the earlier studies, ALEXIS (1993) and FORTE satellite (1997) recorded the pulse pairs which were consisting of exactly two pulses. The pulse pairs were called transionospheric pulse pairs (TIPPs). FORTE satellite observed many TIPPs during the observation period of the satellite [40]. The intervals of a TIPP were longer than tens of microseconds. The first pulse of a TIPP could have its origin above the Earth's surface, and the second pulse could be a reflection of the radiation directed toward the surface from the same source as the first pulse.

The pulses of a TIPP were highly polarized. When a VHF signal propagates through the ionosphere, a linear polarization signal splits into two near-circular polarizations with opposite senses of E-vector rotation. The two modes (ordinary and extraordinary modes) travel at slightly different groups and phase velocities, and result in mode split [41].

The pulse pairs recorded by the VHF sensor differ in the intervals of time between the two pulses consisting TIPP observed by FORTE satellite.

The relationship between the pulse pairs and the mode split is discussed with the numerical calculation of the electromagnetic wave propagation in the following section.

### 4.3.2 Numerical study

The numerical calculation has been made for the characteristics of the radio propagation in the ionosphere to discuss the phenomenon of the pulse pairs observed by the VHF sensor. As the following method, the propagation path and time in the ionosphere are calculated. In this study, the incidence wave is considered as the VHF wideband electromagnetic wave emitted from lightning discharges. The modulated Gaussian pulse by sine wave is used as the incidence wave, which indicates the equation (4.5).

The ionospheric model is used as shown in section 4.2, in order to calculate the characteristics of the radio propagation as discussed above, and the vertical structure of the ionospheric model is rotated around the straight line between the center of the earth and the position of the satellite as in Fig 4.7. The radio wave propagation characteristics are analyzed using the three-dimensional ionospheric mode. The refractive index for electromagnetic wave propagation in cold magnetized plasma is indicated by Appleton-Hartree equation as shown in equation (4.1).

When the equation (4.1) meets the condition of the equation (4.7), it is given by following equation (4.8).

$$\cos^2 \phi \gg -\frac{f^2 f_c \sin^4 \phi}{4(f^2 - f_p^2)^2} \quad (4.7)$$

$$n^2 = 1 - \frac{X}{1 \mp Y \cos \phi} \quad (4.8)$$

In this study, the equation (4.8) to calculate the refractive index in the ionosphere is used. The value of the free electron density  $n_e$  and the earth's magnetism  $B$  are quoted from the IRI-2007 and International Geomagnetic

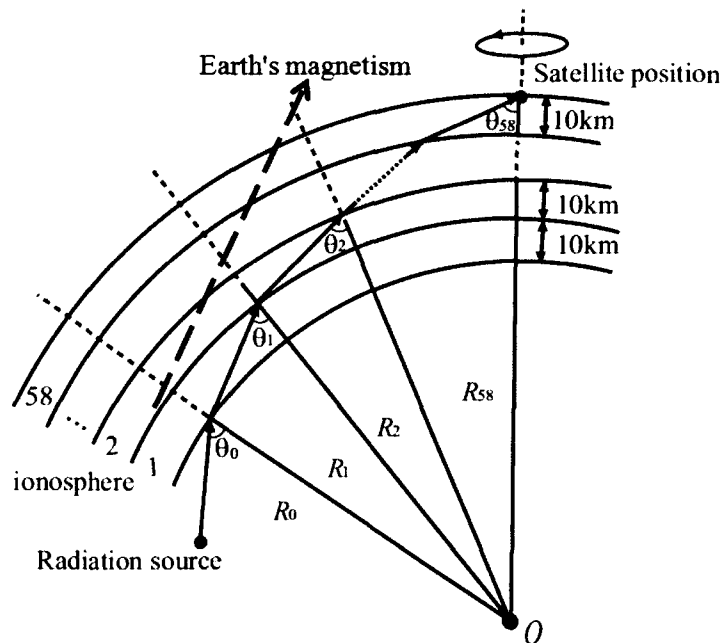


Fig. 4.7 The three-dimensional ionospheric model

Reference Field 10th (IGRF10) at the position of the satellite observation and the time of that. The arrival time difference between the electromagnetic O and X modes by the ray-tracing method is calculated. It is assumed that the altitude of the radiation source is 10 km and that of the satellite is 660 km.

Figure 4.8 shows the overhead view of the analysis range from the position of the satellite. The analysis range is equal to the observation range of the VHF sensor. In Fig. 4.8, the center of the circle  $P_0$  is the satellite position,  $B_s$  is the horizontal component of the Earth's geomagnetic field,  $P_s$  is the position of the radiation source and  $d$  is the distance in a straight line between  $P_0$  and  $P_s$ .  $\theta_s$  is the angle between  $B_s$  and the straight line. In this study, the arrival time difference between the electromagnetic O and X modes is calculated in every 5 km for  $d$  and in every one degree for  $\theta_s$ . The results of the calculation are shown in the next section.

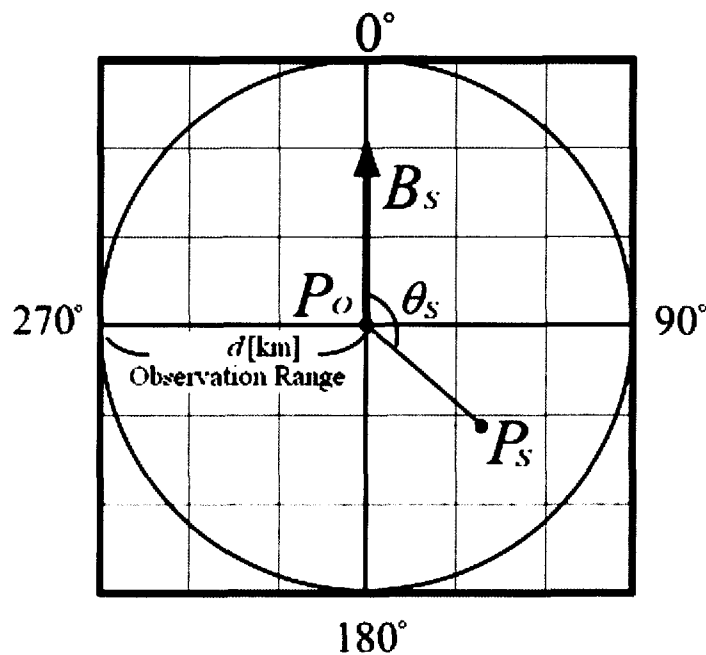


Fig. 4.8 The overhead view of the analysis range from the position of the satellite

### 4.3.3 Discussion about the pulse pairs

The cause of the pulse pairs using the numerical calculation results and the ground-based observation data with WWLLN is discussed. In this study, the observation data with WWLLN for 600 seconds (300 seconds before and after the satellite observation time) are used to know the lightning activity around the satellite observation area. The observed results above Southeast Asia area and Atlantic Ocean area are analyzed. Table 4.1 shows the parameters of the numerical calculation. The parameters are the satellite observation time, the satellite observation position and the value of the earth's magnetism given by IGRF10. Figure 4.9 shows the numerical calculation results and the ground-based observational results with WWLLN in Southeast Asia area. The pulse pair appeared in 20 waveforms of 100 waveforms in this area. In Fig. 4.9, the center of the circle is the position of the satellite. The color bar indicates the arrival time difference between the electromagnetic O and X modes with numerical calculation. The plus sign indicates the location of the lightning activity with WWLLN for 600 seconds (300 seconds before and after the satellite observation time). The results of WWLLN show that there are five lightning activity areas. The areas of A, B, C, D, E, F and G are defined as the lightning activity area. If the radiation source position of the lightning discharge is in the area A, B, C, D, E or F, the

Table 4.1 Numerical calculation parameters

Southeast Asia area	
Observaiton time	24 Feb 18:13:06 2009 UTC
Observaiton point	99.08°E, 0.30°N
Magnetic field (horizon)	34253 nT
Magnetic field (perpendicular)	5952 nT
Atlantic Ocean area	
Observaiton time	10 Jun 02:27:00 2009 UTC
Observaiton point	25.88° W, 7.20 ° N
Magnetic field (horizon)	24888 nT
Magnetic field (perpendicular)	983 nT

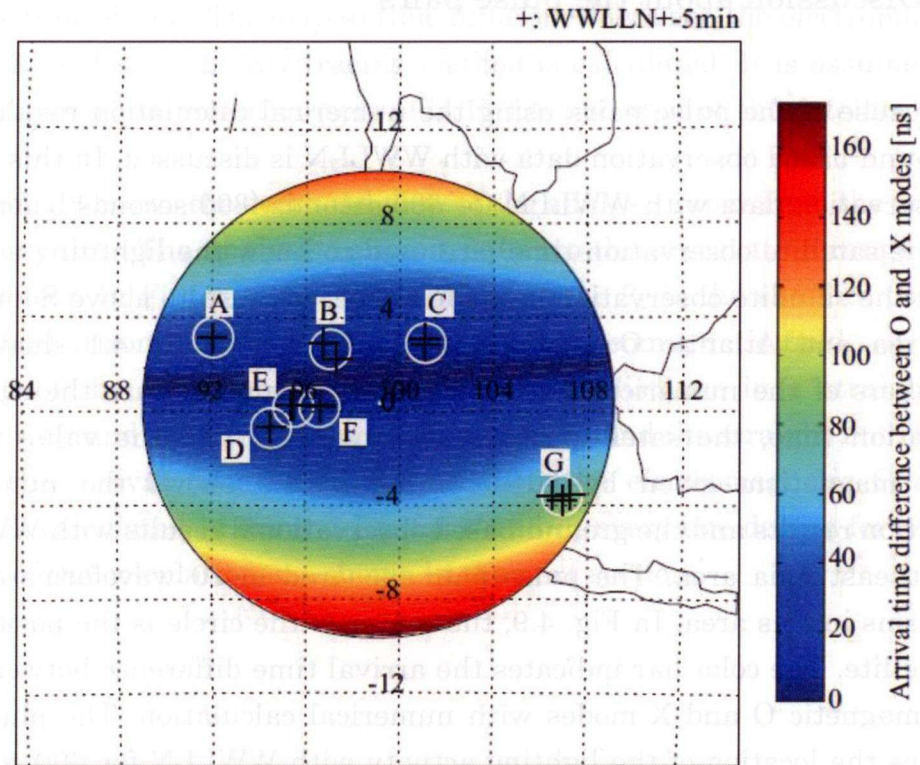


Fig. 4.9 Numerical calculation results and the ground-based observational results with WWLLN in Southeast Asia area

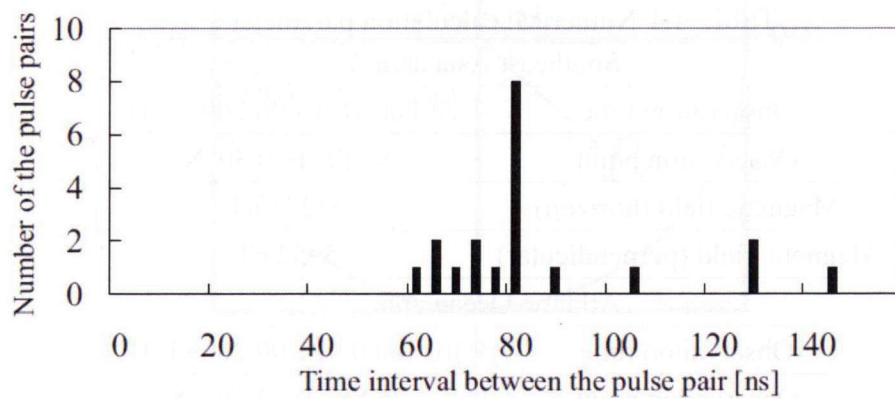


Fig. 4.10 Histogram of the time intervals between the two peaks of the pulses constructed the pulse pair observed with the satellite

arrival time difference between the O and X modes is from 10 ns to 20 ns. On the other hand, if the radiation source position is in the area G, the arrival time difference is about 80 ns. Figure 4.10 shows the histogram of the time intervals between the two peaks of the pulses constructed the pulse pair observed with the satellite. It is often the case that the time intervals are 80 ns. When the radiation source position is in the area G, the time interval between the two pulses corresponds exactly to the numerically calculated arrival time difference between the two modes. These results indicate that the impulsive electromagnetic wave radiated from lightning discharges in area G separates into the O and X modes propagating through the ionosphere. The two pulses with the arrival time difference about 80 ns were received by the VHF sensor as the pulse pairs.

The satellite observation results in Atlantic Ocean area are analyzed. The VHF sensor did not observe the pulse pairs in this area. Figure 4.11 shows

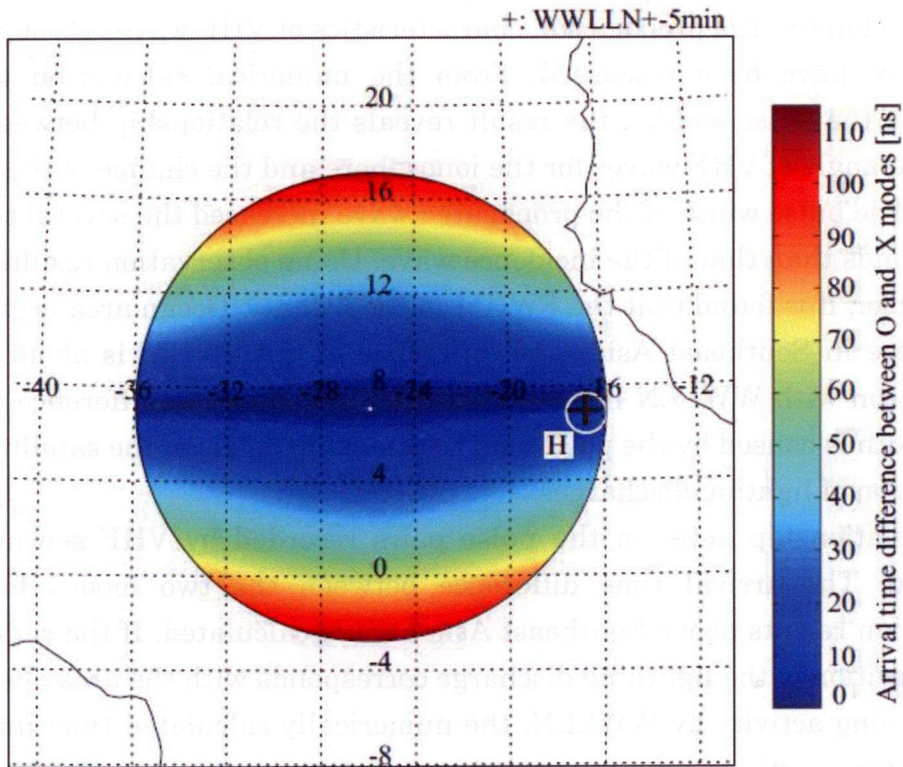


Fig. 4.11 Numerical calculation results and the ground-based observational results with WWLLN in Atlantic Ocean area

the numerical calculation results and the WWLLN observational results in Atlantic Ocean area. The circled area H is defined as the lightning activity area. If the radiation source position of the lightning discharge is in the area H, the arrival time difference between the two modes is from 10 ns to 20 ns. The arrival time differences are not enough to form the pulse pair. This result corresponds with the fact that the VHF sensor did not receive the pulse pairs above this area.

These results are summarized as follows. When the electromagnetic waves (VHF band) with lightning discharges propagate through the ionosphere, they are separated to the two modes. The two pulses with the arrival time difference between O and X modes were received by the VHF sensor as the pulse pairs. It is concluded that the cause of the observed pulse pairs is the mode split.

#### 4.4 Conclusion

In this chapter, the propagation characteristics of VHF waves through the ionosphere have been discussed. From the numerical calculation of the change of the pulse widths, the result reveals the relationship between the incidence angle of VHF waves for the ionosphere and the change of the pulse widths. The pulse width of the propagated wave increased the several tens of nanoseconds than that of the incidence wave. Using observation results with VHF sensor, it is found that the FWHM in the Atlantic Ocean area is greater than those in Southeast Asia. The difference of the FWHM is about 5 ns. Comparison with WWLLN lightning location indicates the difference of the pulse width is caused by the positional relationship between the satellite and the location of lightning discharges.

The relationship between the pulse pairs recorded by VHF sensor was discussed. The arrival time difference between the two modes for the observation results above Southeast Asia area is calculated. If the radiation source position of the lightning discharge corresponds with the area observed the lightning activity by WWLLN, the numerically calculated time interval corresponds exactly to time intervals between the observed pulse pairs. And then, in Atlantic Ocean area, the VHF sensor did not observe the pulse pairs above this area. The numerically calculated arrival time difference between the two modes is about 20 ns. The arrival time difference is not enough to

form the pulse pair. This result corresponds with the fact that the VHF sensor did not receive the pulse pairs above this area.

These results are summarized as follows. When the electromagnetic waves (VHF band) with lightning discharges propagate through the ionosphere, they are separated to the two modes. The two pulses with the arrival time difference between O and X modes are received by the VHF sensor as the pulse pairs. It is concluded that the cause of the observed pulse pairs is the mode split.



# Chapter 5

## VHF broadband interferometer on the ISS

### 5.1 Introduction

In this chapter, the overview of the global lightning and sprite measurements (GLIMS) mission is described [18]. The GLIMS is a mission on the international space station (ISS) to detect and locate optical transient luminous events (TLEs) and associated lightning simultaneously from the non-sun-synchronous orbit. The objectives are to clarify the conditions which

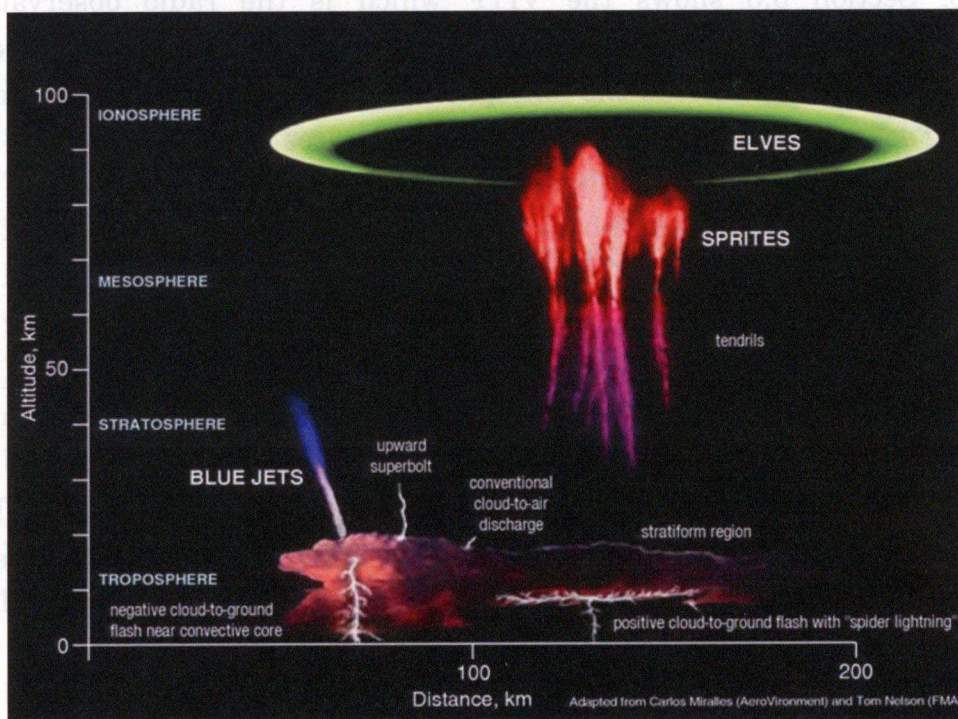


Fig.5.1 Transient Luminous Events (TLEs) such as red sprites, elves, blue jets, halo or trolls. TLEs are upper atmospheric optical phenomena associated with thunderstorms [Graphic courtesy of Carlos Miralles (AeroVironment) and Tom Nelson (FMA)].

TLEs occur, the global occurrence rates and distributions of TLEs, the mechanism by which terrestrial gamma-ray flashes (TGFs) occur and their relation to lightning discharges, as well as to locate the sources of VHF radiation emitted by lightning. TLEs are reported to be associated with the CG lightning with large amount of positive charge [42], [43]. In addition, the TLEs have been classified into a few categories and named sprites, blue jets, and elves according to their morphology as shown in Fig. 5.1. The mechanism by which TLEs are generated is not yet fully understood. The most promising explanation so far is the quasi-static electric field model. However, this model also has several problems in point of the charge moments which real TLEs can be generated [44], [45].

The VHF broadband digital interferometer (VITF) on GLIMS in detail is described. The VITF is developed to estimate the arrival direction of electromagnetic waves from lightning discharges using interferometric technique.

Section 5.2 presents the optical and radio observation instruments on GLIMS. Section 5.3 shows the VITF which is the radio observation instrument developed to estimate the arrival direction of electromagnetic waves. Section 5.4 describes the ionospheric effect on the determination of lightning source location using VITF and summarizes this chapter.

## 5.2 Observation Instruments on JEM-GLIMS

### 5.2.1 GLIMS mission

To clarify the temporal and spatial relationship between the TLEs and the lightning discharges, the following instruments are installed on the ISS. The observation instruments of the lightning and TLEs are the Lightning and Sprite Imager (LSI), Photometers (PHs), a VLF Receiver (VLFR), and a VHF Interferometer (VITF) as shown in Fig. 5.2. These instruments have the following characteristics [46], [47].

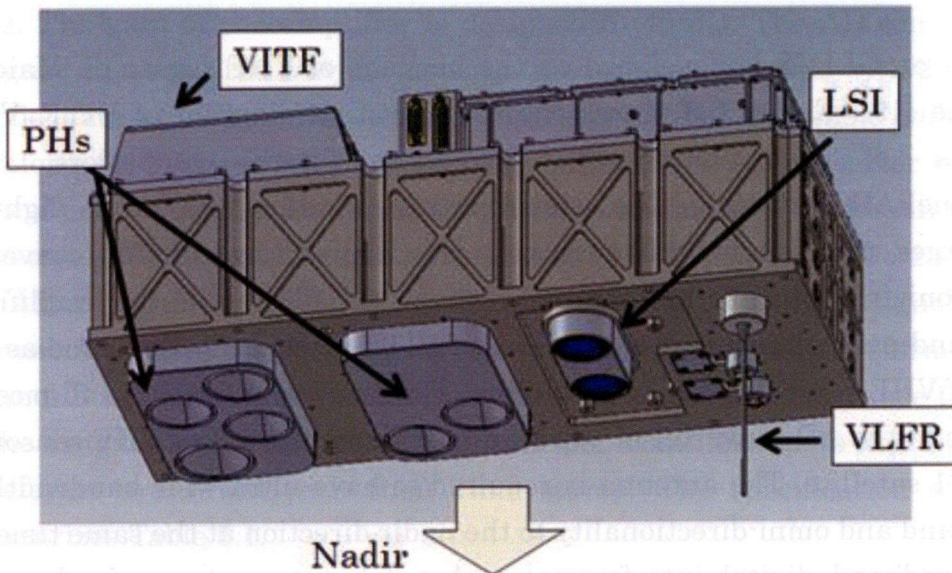


Fig. 5.2 The instruments on GLIMS. The Lightning and Sprite Imager (LSI), Photometers (PHs), a VLF Receiver (VLFR), and a VHF Interferometer (VITF)

- LSI (optical instrument): The LSI consists of two CMOS cameras with filters at different wavelengths, as well as staring imagers to identify TLEs and lightning by detecting transient changes in light intensity.
- PH (optical instrument): The PHs are designed to record the absolute light intensity emitted by TLEs and lightning at six different wavelengths in the ultraviolet and the near infrared region.
- VLF (radio instrument): The VLFR is an electromagnetic wave receiver at the VLF band from 1 to 40 kHz to measure the whistler wave emitted by lightning discharge
- VITF (radio instrument): The VHF interferometer will be the first lightning location system on the VHF band in space.

These instruments of GLIMS were launched in July 2012 and installed on the ISS at an altitude of 400 km circular orbit with 50 degree inclination angle. The mission is scheduled to observe the lightning and TLEs at least 3 years.

## 5.2.2 VHF Interferometer

VITF on GLIMS is developed on the heritage of VHF sensor on Maido-1 satellite [19]. Figure 5.3 shows the configuration diagram of VITF. VITF consists of two antennas, band-pass filters, amplifiers, and 2-channel-AD-converter. The electromagnetic radiations from lighting discharges received by the antennas are digitized by the AD converter synchronizing with another channel through the filters and the amplifiers. The band-pass filter and the amplifier of VITF are exactly the same as the ones of VHF sensor on Maido-1 satellite. The basic specification and most of devices in the AD converter of VITF are proven by the one of VHF sensor on Maido-1 satellite. The antenna is required to have ultra-wide bandwidth in VHF band and omni-directionality to the nadir direction at the same time for the broadband digital interferometry. A patch type antenna is designed within the size of  $200 \times 200$  mm. The same two units of antennas are installed at the both ends of the Multi-mission Consolidated Equipment (MCE) with the separation of 1.6 m. Their bandwidths with the higher return loss than -3 dB are from 70 to 100 MHz. The band-pass filter and the amplifier of VITF are the copies of the ones of VHF sensor on Maido-1 satellite. 3 dB pass

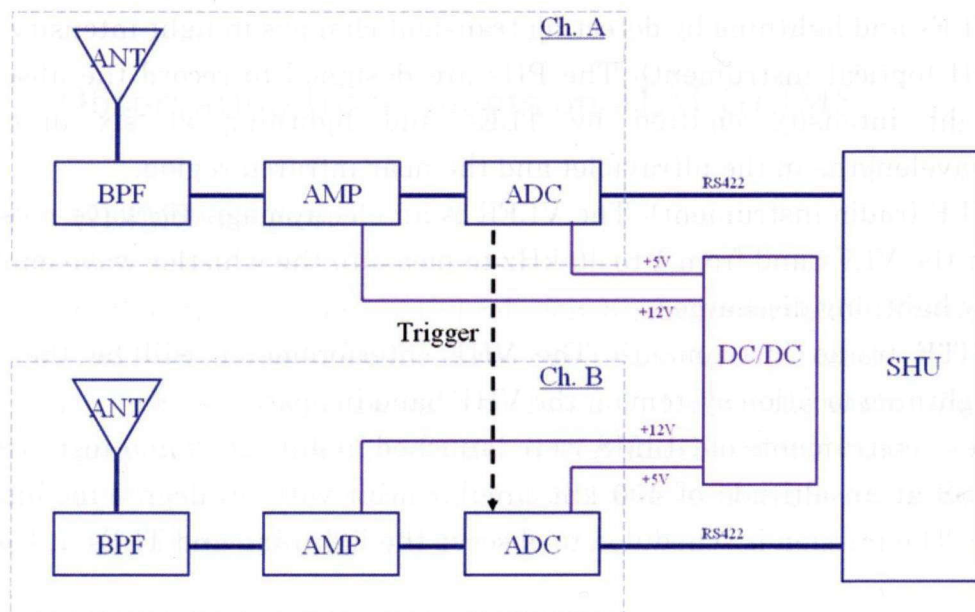


Fig. 5.3 The configuration diagram of VITF

band of the filter is from 30 to 100 MHz with 20 dB attenuation at 20 and 110 MHz. The gain of the amplifier is designed to 45 dB. The AD converter is designed to record 130 waveforms with the duration of 2.5  $\mu$ s with 200 MS/s as one dataset. When the input signal exceeds the threshold voltage, a waveform for 2.5  $\mu$ s is stored on the ring-buffer of the AD converter with the 25 % of pre-triggering. The basic specification and most of devices in the AD converter of VITF are the same as the one of VHF sensor on Mado-1 satellite. The AD converter is expanded two channels in VITF. The input signal to the channel A is used for detection of the triggering and the waveform of the channel B is recorded in synchronization with the channel A. Since the size of the ring-buffer is for 130 waveforms per channel, up to the last 130 waveforms are saved with their time stamp. The specification of VITF summarizes Table 5.1.

Table 5.1 Specification of VITF

Band-pass filter	
3 dB pass band	30 ~ 100 MHz
Insertion loss	-1 dB (at center frequency)
Attenuation	-20 dB / 20, 110 MHz
In-and out-put impedance	50 $\Omega$
Amplifier	
Input level	-85 ~ -35 dBm
Gain	45 dB
Output level	1 Vp-p
In-and out-put impedance	50 $\Omega$
AD converter	
Data sampling speed	200 MS/s
AD resolution	8 bit
Input channel	2
Triggering	Level trigger system
Threshold level	50 ~ 500 mV (10 steps variable)
Memory	130 $\times$ 2.5 $\mu$ s

## 5.3 Evaluation of the estimation error of VITF

### 5.3.1 Simulation of the ionospheric effect

When the arrival direction of electromagnetic waves is estimated by VITF on the ISS, it is necessary to consider the estimation error caused by the ionosphere. The value obtained using the interferometric technique is an incidence angle of electromagnetic waves for the antenna. The relationship between the incidence angle and the location of the radiation source is represented by the following two cases as shown in Fig. 5.4.

- ① We do not consider the refraction in the ionosphere (solid line in Fig.5.4).
- ② We consider the refraction in the ionosphere in the day-and-nighttime (dotted line in Fig.5.4).

Where, the case of ① means that the location of the radiation source is estimated without correcting the arrival direction of electromagnetic waves obtained by the interferometric technique. The case of ② means that the

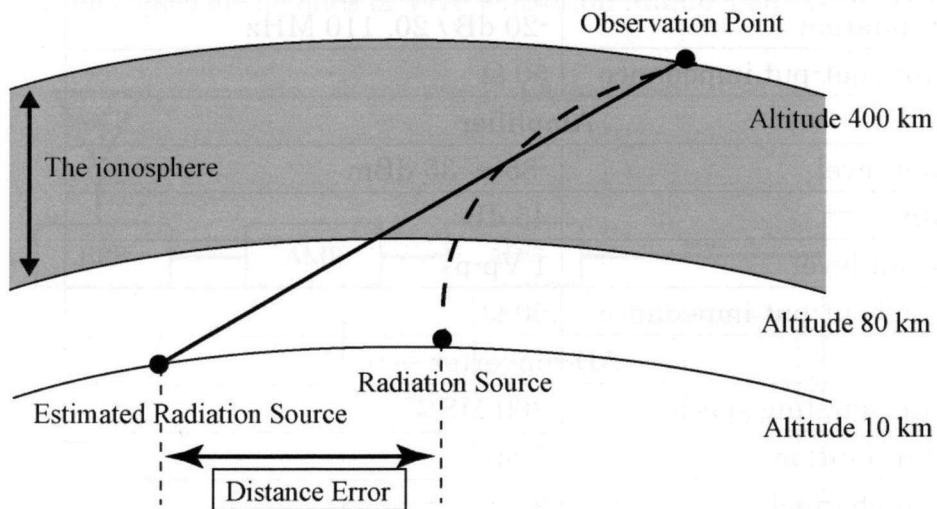


Fig. 5.4 The illustration of the evaluating method of the estimated error (not to scale). The solid line indicates the propagation path without consideration of refraction effects in the ionosphere. The dashed line is the calculated propagation path using the ionosphere model.

propagation path is the real propagation path considering the refraction in the ionosphere. The above two types of the propagation path are calculated respectively, and comparing the locations calculated with and without the effect of ionospheric refraction, the difference of distance is estimated as an error which terms 'distance error' in this paper. If the distance error is more than 10 km, the estimation result of the arrival direction of electromagnetic waves needs to be corrected because the scale of thunder cloud is a dozen kilometers. The analysis range of incidence angle is from  $0^\circ$  to  $65^\circ$  considering that the maximum value of incidence angle is the field of view of  $65^\circ$  from the observation altitude of 400 km.

### 5.3.2 Methodology

The ionospheric model is used in order to calculate the distance error of the radio propagation path as discussed in Section 4.2.1. In this section, the value of the electron density in each layer is calculated by IRI-2012. The electron density varies with the time and the location (latitude and longitude). This paper has focused on the electron density at the day-and-nighttime to analyze the effect of the ionosphere for the distance error.

The altitude distribution of electron density at the day-and-nighttime in one year of 2012 is indicated as shown in Fig.5.5 (a). The figure indicates the annual average of the electron density at 12 o'clock in the daytime and 0 o'clock in the nighttime in local time in the location where both the latitude and the longitude are 0 degree, where the error bar shows the standard deviation. The electron density in the daytime is relatively higher than that in the nighttime. Especially, the value in the daytime is about ten to hundred times than that in the nighttime at the altitude from 100 km to 200 km. Fig.5.5 (b) shows the variation of the refractive index in the day-and-nighttime ionosphere calculated from the altitude distribution of the electron density in Fig.5.5 (a), where the frequency of the electromagnetic waves is 70 MHz. This figure indicates that the refractive indices in the daytime largely vary at the altitude of 250 km to 450 km where the electron density is high. The variations of the refractive indices in the nighttime are relatively small. From these results it is evident that the

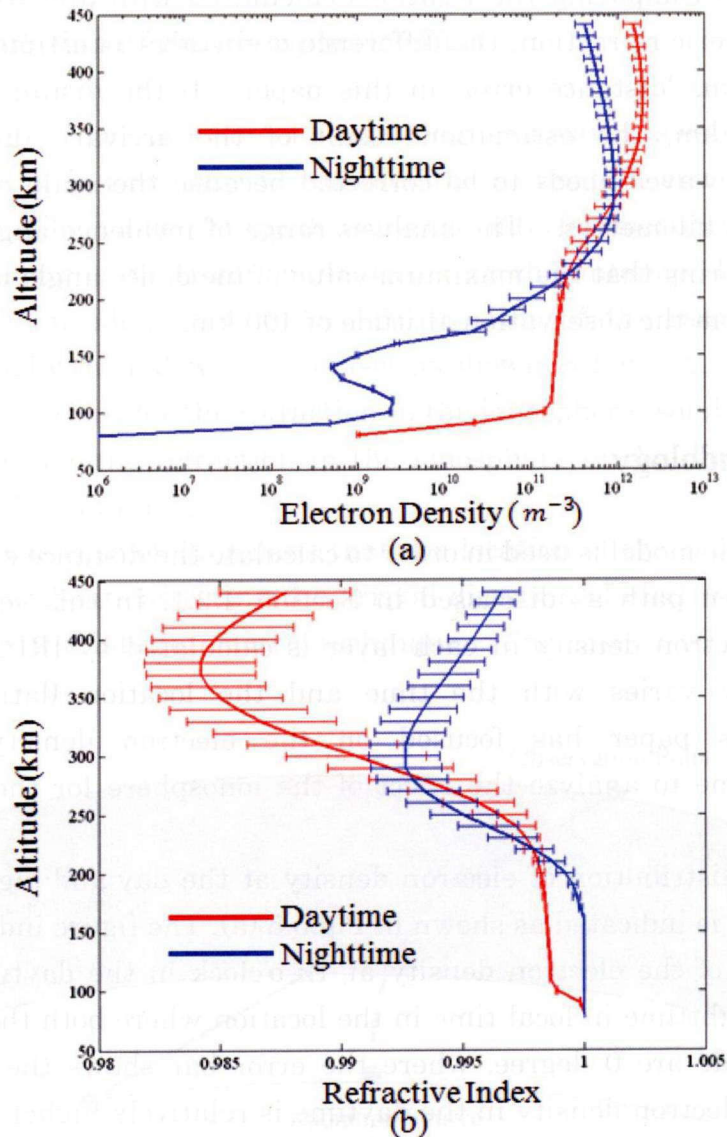


Fig. 5.5 The altitude distribution of the electron density and the refractive index. (a) The altitude distributions of the electron density in daytime ionosphere and nighttime ionosphere. The blue and red lines indicate the mean value of the electron density at nighttime and daytime in a year respectively. (b) The refractive indices of the daytime ionosphere and nighttime ionosphere calculated with the electron density distribution.

ionosphere influences the propagation path of radio waves at the altitude of 200 km to 400km. Another considerable factor regarding the electron density in the ionosphere is solar activity. Solar activity varies with about a cycle of 11 years. Considering the result, the rising part of solar activity will be expected after 2012 [48]. In this paper, the annual average value of electron density for each layer as an initial value is used in this thesis.

### 5.3.3 Results and discussion

Figure 5.6 shows the results of numerical calculation for the incidence angle to the antenna located at an altitude of 400 km and for the distance error. The dashed line and the solid line indicate the estimated error in the daytime ionosphere and the nighttime ionosphere, respectively. The altitude distribution of electron density at the place where both the latitude and longitude equal  $0^\circ$  is used as an initial value. It is considered that there is almost no error in the case of electron density in ionosphere in the nighttime comparing with the result without the consideration of the refraction. Even in the case of incidence angle of  $65^\circ$  that the error is the largest, the error value is 1 km and very small, while the distance error in the ionospheric condition of the daytime starts to rise at the incidence angle of  $20^\circ$ , and become about 5 km at  $50^\circ$ , about 15 km at  $60^\circ$  and about 35 km at  $65^\circ$ .

In general, it is well known that the effect of the refraction in the ionosphere on the electromagnetic waves of VHF band is not so large. This is because the frequency range of VHF band (70-100MHz) is much larger than the plasma frequency that is normally several MHz, and the influence of the plasma vibration is small.

In fact it is clear from the present numerical result that the effect of refraction in the ionosphere can be ignored in the nighttime. In the daytime ionospheric condition, however, it was found that the distance error becomes several dozen kilometers with the increase of incidence angle. The reason is that the propagation path in the ionosphere becomes long with increase of incidence angle. Especially, the propagation distance reaches about 1300 km when the incidence angle is  $65^\circ$ . The observation result from the Mado-1 satellite showed that the propagation distance was more than 1300 km when the wide band electromagnetic waves of 30 to 100 kHz were received at the altitude of 660 km. This means that it is necessary to consider the refraction of the propagation path in the frequency of VHF band in the daytime ionosphere at an ISS altitude of 400 km.

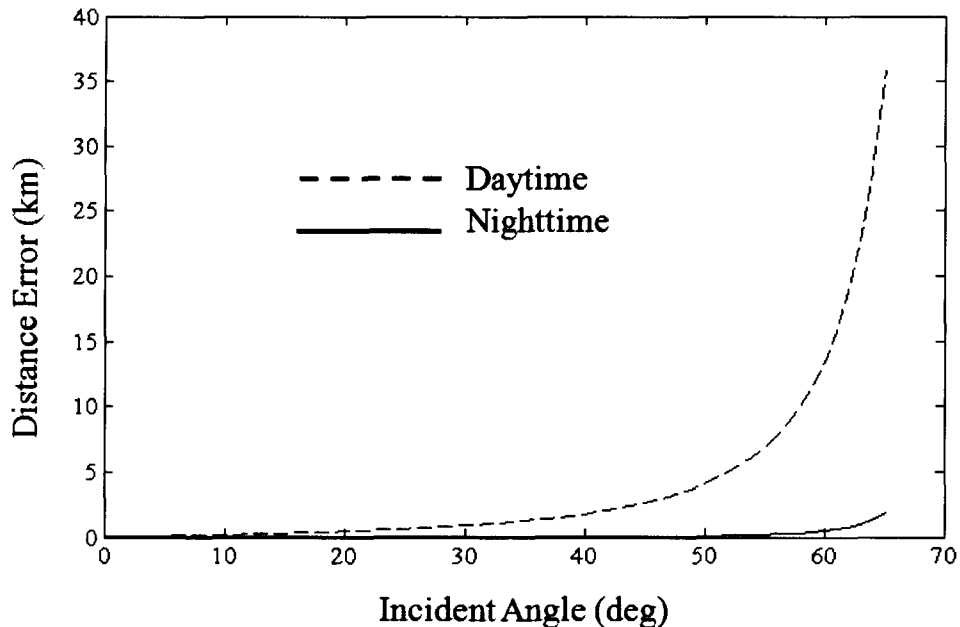


Fig. 5.6. The distance error for the incident angle of the waves. The dashed line and the solid line indicate the estimated error in the daytime ionosphere and the nighttime ionosphere respectively.

The variation of electron density at the observation point is discussed. In foregoing section the observation point was the place where both the latitude and longitude is  $0^\circ$ . The ionosphere indicates the various electron density distributions at the observation point all over the world. In order to discuss the distribution quantitatively, the annual average of the electron density distribution was determined using the IRI-2012 model for every ten degrees of latitude and longitude shown in Fig. 5.7. Where, the color bar is the value of Total Electron Continents (TEC) for vertical direction.

As the distance error is very small from the discussion of foregoing section in the nighttime electron density, we analyze it in the daytime electron density in this section. The analysis range is set from  $-50^\circ$  to  $50^\circ$  in the latitude direction considering the orbit of the ISS. From Fig.5.7, the high electron density region is found near the equator. The distance error is determined as same as the forgoing section using an initial value that is the annual average value for the latitude and longitude of every ten degrees.

The values of distance error for the incidence angles of  $55^\circ$ ,  $60^\circ$  and  $65^\circ$  are

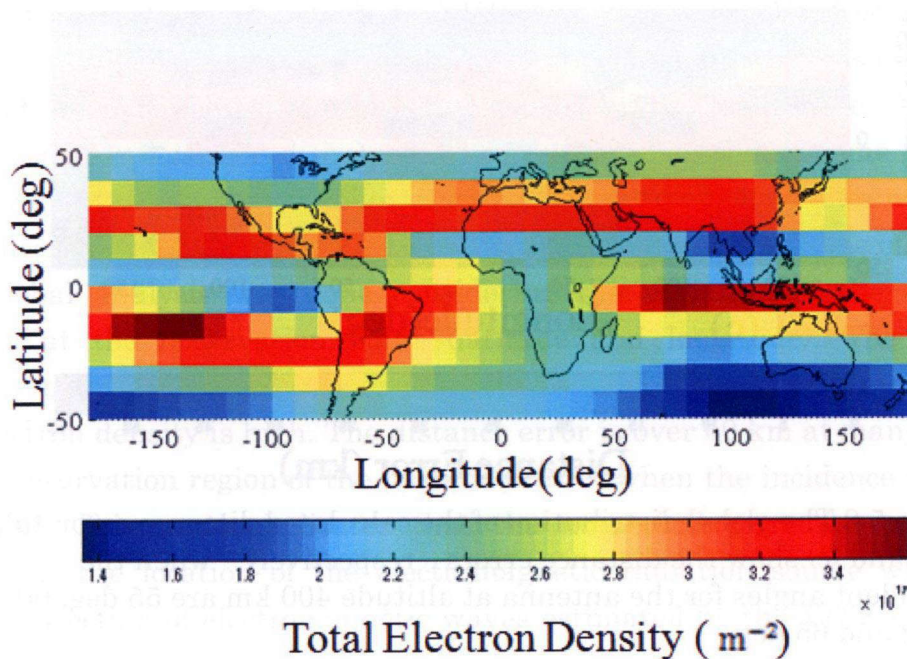


Fig. 5.7 The global distribution of the vertical Total Electron Density (TEC) . The value of the vertical TEC is the yearly average.

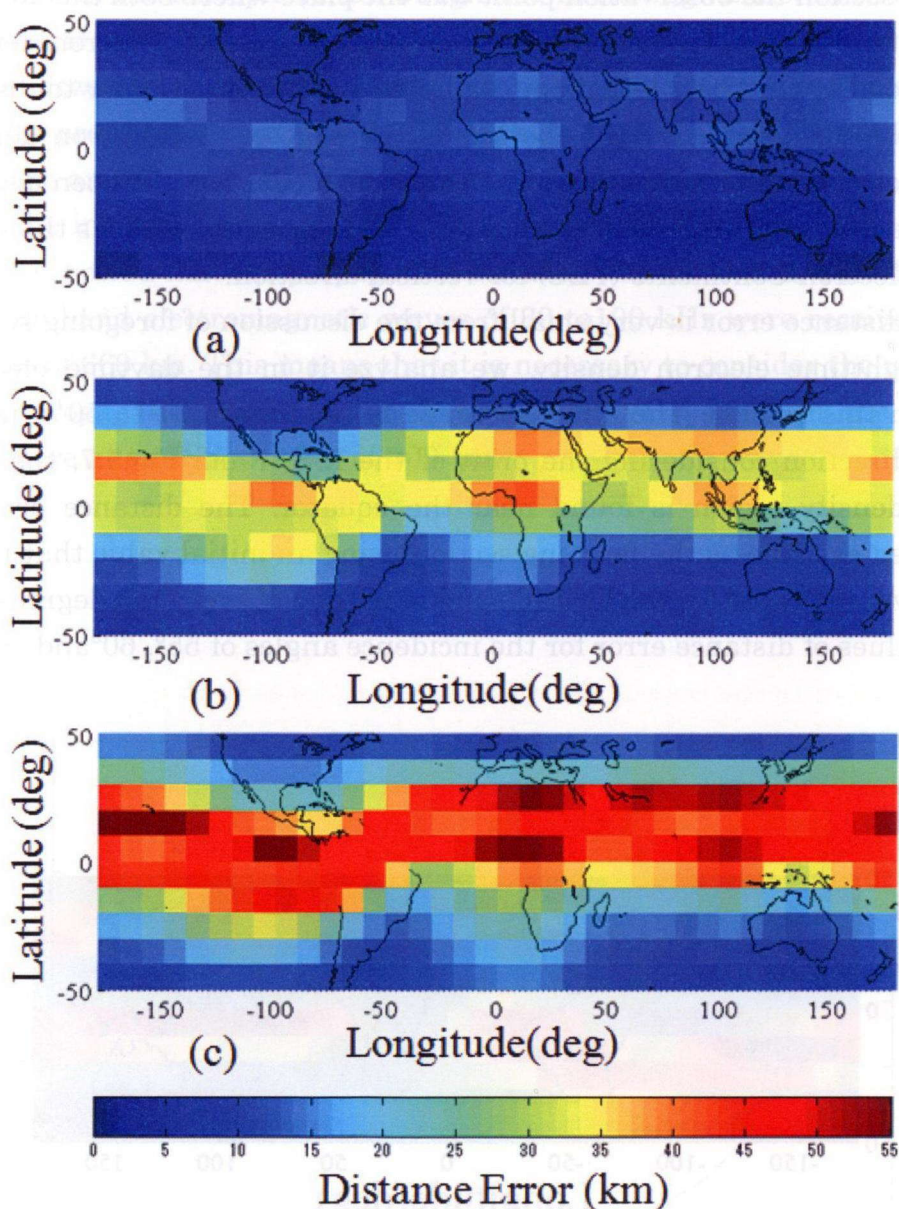


Fig. 5.8 The global distribution of the calculated distance error. (a), (b) and (c) show the distance errors respectively when the incident angles for the antenna at altitude 400 km are 55 deg, 60 deg and 65 deg.

shown in Fig.5.8 (a), (b) and (c). Where, the color bar indicates the distance error. From Fig.5.8 (a), in the case that the incidence angle is under  $55^\circ$ , the distance error is very small (a few km) so it is not considered the influence of ionosphere. From Fig.5.8 (b), in the case of the incidence angle of  $60^\circ$ , the distance error is more than 25 km near the equator in the region of the latitude of  $\pm 25^\circ$  and also it is less than 20 km in the other region. From Fig.5.8 (c), in the case of the incidence angle of 65 degree, the distance error is more than 40 km in the region of the latitude of  $\pm 35^\circ$ .

From these results, the correction of the distance error is needed in the most analysis region (the latitude of  $\pm 50^\circ$ ) over the incidence angle of  $60^\circ$ . And also the distance error increases rapidly and reaches to the maximum value of 55 km when the incidence angle approaches to  $65^\circ$ .

## 5.4 Conclusion

In this chapter, the overview of the GLIMS mission and the VHF radio observation instrument which is VHF Interferometer (VITF) has been presented. When the arrival direction of electromagnetic waves is estimated by VITF on ISS, the estimation error caused by the ionosphere using the numerical calculation is discussed. The results using the daytime electron density distribution indicated that the distance error is 30~35 km when the incidence angle is  $60^\circ$  to  $65^\circ$  for the antenna located at the altitude of 400 km. The global analysis was done considering the variation of the electron density at the observation point (latitude and longitude). The results indicate that the incidence error is relatively large near the equator where the electron density is high. The distance error is over 40 km at many places in the observation region of the latitude of  $\pm 50^\circ$  when the incidence angle is over  $60^\circ$ . This result indicates that the numerical correction needs to determine the location of the electromagnetic radiation source when the arrival direction of electromagnetic waves estimated by the VITF is in this range.

In GLIMS mission, the simultaneous observations of optical and radio instruments will be conducted. We will also compare the optical data of lightning discharge with the arrival estimation results of the VITF.



# Chapter 6

## Conclusion

This thesis has presented about the radio observation on lightning discharges from space. In order to realize the space-borne VHF broadband digital interferometer (DITF), the VHF sensor carried on the Maido-1 satellite had developed and observed the lightning discharges from space. From the observation results and numerical calculations, the propagation characteristics of VHF waves in the ionosphere have been discussed.

Chapter 1 has presented the overview and the objective of this thesis. The need for the monitoring details of lightning discharges which are useful to prevent the weather disasters was described. The existing lightning location systems and the advantages of the space-borne VHF DITF were presented.

Chapter 2 has described the configurations of the Maido-1 satellite and VHF sensor in detail. The VHF sensor on Maido-1 satellite had conducted 158 lightning observations all over the world and proved its function in space. There seems to have been regional difference of frequency of lightning. In previous study, the Optical transient detector (OTD) and Lightning imaging sensor (LIS) indicated the distribution of lightning on the globe. The results indicate the frequency of the lightning activity is higher on shore than at sea. These results show that it is possible to observe lightning activities using radio wave from satellite orbit.

Chapter 3 has described the temporal and spatial comparison with World Wide Lightning Location Network (WWLLN). It was found that the coincidence rates in the North and South American continents, and in Southeast/East Asia and the Australian continent were greater than 0.90. On the other hand, the coincidence rates in the African and European continents and in the Pacific and Atlantic Oceans were less than 0.61. Considering the regional difference of the detection efficiency of the WWLLN, the VHF sensor events agree with the WWLLN events. In addition, the 6 coincident VHF sensor events were analyzed in detail. The incidence angles

for VHF sensor were estimated by numerical simulation. Compared with WWLLN events, the difference is within 1 degree. The temporal and spatial coincidences show a clear relationship between the VHF sensor events and the lightning discharges.

Chapter 4 has described the wave propagation characteristics in the ionosphere. The change of the pulse width of the Electromagnetic (EM) waves propagated through the ionosphere was calculated. The pulse width increased the several tens of nanoseconds than that of the incidence wave. From the observed waveforms, it was found that the difference of the pulse width is caused by the positional relationship between the satellite and the location of lightning discharges.

The cause of the observed pulse pairs was also discussed with the numerical calculation. The numerically calculated time interval of the pulse pairs corresponds exactly to that of the observed pulse pairs. The results are summarized as follows. When the electromagnetic waves radiated from lightning discharges propagate through the ionosphere, they are separated to the ordinary and extraordinary modes.

Chapter 5 has presented the VHF broadband interferometer (VITF). The arrival direction of EM waves was estimated using the VITF on the international space station (ISS). The numerical calculations indicate that the effect of refraction in the ionosphere can be ignored in the nighttime. In the daytime ionospheric condition, the distance error becomes several dozen kilometers when the incidence angle is  $60^\circ$  to  $65^\circ$  for the antenna. It is also indicated that the distance error is relatively large near the equator. The distance error is over 40 km in the latitude of  $\pm 50^\circ$  when the incidence angle is over  $60^\circ$ . These results indicate that the numerical correction is needed to determine the location of the EM radiation source estimated by interferometer in this range.

This thesis contributes to the field of the atmospheric electricity to understand the propagation of electromagnetic waves radiated from lightning discharges. The results using the VHF sensor on the Mado-1 satellite and some numerical calculations increase effectiveness of the space-borne VHF DITF. In the future, we will develop the space-borne VHF DITF. It will give us the information of the location of thunder storms all over the world, constantly. It will be also expected to contribute the disaster prevention.

# List of Acronyms

---

ADC	Analog-to-digital converter
AMP	Amplifier
BPF	Band-pass filter
CG	Cloud-to-ground
DITF	Broadband digital interferometer
ELF	Extremely low frequency
EM	Electromagnetic
FORTE	Fast on-orbit recording of transient events
FOV	Field of view
FWHM	Full width at half maximum
GLIMS	Global lightning and sprite measurements
IC	Intracloud
IGRF10	International geomagnetic reference field 10 <sup>th</sup>
IQR	Interquartile range
IRI	International reference ionosphere
ISS	International space station
JAXA	Japan aerospace exploration agency
JEM-EF	Exposed facility of japanese experiment module
LF	Low frequency
LIS	Lightning imaging sensor
LRG-OU	Lightning research group of Osaka University
LSI	Lightning and sprite imager

---

---

MCE	Multi-mission consolidated equipment
O mode	Ordinary mode
OTD	Optical transient detector
PHs	Photometers
SMEs	Small-and-medium-sized manufacturing enterprises
STFT	Short term fourier transform
TEC	Total electron content
TGFs	Terrestrial gamma-ray flashes
TIPPs	Transionospheric pulse pairs
TLEs	Transient luminous events
TOGA	Time of group arrival
UEs	Undetectable events
VHF	Very high frequency
VITF	VHF broadband interferometer
VLFR	VLFR receiver
WWLLN	World wide lightning location network
X mode	Extraordinary mode

---

# Bibliography

- [1] Finke, U and O. Kreyer (2002), Detect and Locate Lightning Events from Geostationary Satellite Observations: Report Part I Review of existing lightning location systems (2002), MTG Reports from EUMETSAT Scientific studies and workshops.
- [2] Cummer, S. A., G. Lu, M. S. Briggs, V. Connaughton, S. Xiong, G. J. Fishman, and J. R. Dwyer (2011), The lightning-TGF relationship on microsecond timescales, *Geophys. Res. Lett.*, 38, L14810.
- [3] Akita, M., S. Yoshida, Y. Nakamura, T. Morimoto, T. Ushio, Z.-I. Kawasaki, D. Wang (2011), Effects of Charge Distribution in Thunderstorms on Lightning Propagation Paths in Darwin, Australia. *J. Atmos. Sci.*, 68, 719–726.
- [4] Yoshida, S., M. Akita, T. Ushio, Z.-I. Kawasaki (2011), Propagation characteristics of lightning stepped leaders developing in charge regions and descending out of charge regions, *Atmospheric Research*, 106, 86-92.
- [5] Thomas, R. J., P. R. Krehbiel, W. Rison, T. Hamlin, J. Harlin, and D. Shown (2001), Observations of VHF source powers radiated by lightning, *Geophys. Res. Lett.*, 28(1), 143–146.
- [6] Biagi, C. J., K. L. Cummins, K. E. Kehoe, and E. P. Krider (2007), National Lightning Detection Network (NLDN) performance in southern Arizona, Texas, and Oklahoma in 2003–2004, *J. Geophys. Res.*, 112, D05208.
- [7] Lay, E. H., R. H. Holzworth, C. J. Rodger, J. N. Thomas, O. Pinto Jr., and R. L. Dowden (2004), WWLL global lightning detection system: Regional validation study in Brazil, *Geophys. Res. Lett.*, 31, L03102.

- [8] Smith, D. A., M. J. Heavner, A. R. Jacobson, X. M. Shao, R. S. Massey, R. J. Sheldon, and K. C. Wiens (2004), A method for determining intracloud lightning and ionospheric heights from VLF/LF electric field records, *Radio Sci.*, 39, RS1010.
- [9] Dowden, R.L., J.B. Brundell and C.J. Rodger (2002), VLF lightning location by time of group arrival (TOGA) at multiple sites, *Journal of Atmospheric and Solar-Terrestrial Physics*, 64, 817-830.
- [10] Buechler, D. E., K. T. Driscoll, S. J. Goodman, and H. J. Christian (2000), Lightning activity within a tornadic thunderstorm observed by the optical transient detector (OTD), *Geophys. Res. Lett.*, 27(15), 2253–2256
- [11] Boccippio, D. J. , S. J. Goodman, S. Heckman (2000), Regional Difference in Tropical Lightning Distributions, *Journal of Applied Meteorology*, 39, 2231-2248.
- [12] Jacobson, A. R., S. O. Knox, R. Franz, and D. C. Enemark (1999), FORTE observations of lightning radio-frequency signatures: Capabilities and basic results, *Radio Sci.*, 34(2), 337–354.
- [13] Jacobson, A. R., K. L. Cummins, M. Carter, P. Klingner, D. R. Dupré, and S. O. Knox (2000), FORTE radio-frequency observations of lightning strokes detected by the National Lightning Detection Network, *J. Geophys. Res.*, 105(D12), 15,653–15,662
- [14] Morimoto, T., A. Hirata, Z.-I. Kawasaki, T. Ushio, A. Matsumoto, Akinori and J. Lee (2005), An Operational VHF Broadband Digital Interferometer for Lightning Monitoring, *IEEEJ Transactions on Fundamentals and Materials*, 124, 12, 1232-1238.
- [15] Kikuchi, H., T. Morimoto, T. Ushio and Z.-I. Kawasaki (2010), Wideband radio wave observations of lightning discharge by Mado-1 satellite, *IEICE Transactions on Communications*, E93-B, 8, 2226-2227.

- [16] Kikuchi, H., S. Yoshida, T. Morimoto, T. Ushio and Z.-I. Kawasaki (in press), VHF Radio Wave Observations by Mado-1 Satellite and Evaluation of its Relationship with Lightning Discharges, IEICE Transactions on Communications.
- [17] Kikuchi, H., S. Yoshida, T. Morimoto, T. Ushio and Z.-I. Kawasaki (2010), Satellite Observations for Lightning Discharges and Analysis of VHF Electromagnetic Waveforms, IEEJ. Transactions on Fundamentals and Materials, 131, 9, 705-710.
- [18] Ushio, T., M. Sato, T. Morimoto, M. Suzuki, H. Kikuchi, A. Yamazaki, Y. Takahashi, Y. Hobara, U. Inan, I. Linscott, Y. Sakamoto, R. Ishida, M. Kikuchi, K. Yoshida, Z.-I. Kawasaki (2011), The Global Lightning and Sprite Measurement (GLIMS) Mission of the International Space Station - Concept and Overview, IEEJ. Transactions on Fundamentals and Materials, 131, 12, 971-976.
- [19] Morimoto, T., H. Kikuchi, M. Sato, M. Suzuki, A. Yamazaki, and T. Ushio (2011), VHF Lightning Observations on JEM-GLIMS Mission -Gradual Approach to Realize Space-borne VHF Broadband Digital Interferometer-, IEEJ. Transactions on Fundamentals and Materials, 131, 12, 977-982.
- [20] Kikuchi, H., S. Yoshida, T. Morimoto, T. Ushio and Z.-I. Kawasaki (in press), The ionospheric effect on the determination of lightning source location using VHF radio waves by satellite remote sensing (in Japanese). IEEJ. Transactions on Fundamentals and Materials
- [21] Nakamura, Y., and H. Hashimoto (2005), SOHLA-1, A low cost satellite development with technology transfer program of JAXA, Proceedings of 56th IAC (International Astronautical Congress) 2005, IAC-05-B5.6.B.08.
- [22] Christian, H. J., R. J. Blakeslee, D. J. Boccippio, W. L. Boeck, D. E. Buechler, K. T. Driscoll, S. J. Goodman, J. M. Hall, W. J. Koshak, D. M. Mach and M. I. F. Stewart (2003), Global frequency and distribution of lightning as observed from space by the Optical Transient Detector, J. Geophys. Res., 108(D1), 4005.

- [23] Lay, E.H., R.H. Holzworth, C.J. Rodger, J.N. Thomas, O. Pinto Jr and R.L. Dowden (2004), WWLL global lightning detection system: Regional validation study in Brazil, *Geophysical Research Letters*, 31, L03102.
- [24] Rodger, C.J., S. Werner, J.B. Brundell, E.H. Lay, N.R. Thomson, R.H. Holzworth, and R.L. Dowden (2006), Detection efficiency of the VLF World-Wide Lightning Location Network (WWLLN): initial case study, *Ann. Geophys.*, 24, 3197-3214.
- [25] Abreu, D., D. Chandan, R.H. Holzworth, and K. Strong (2010), A performance assessment of the World Wide Lightning Location Network (WWLLN) via comparison with the Canadian Lightning Detection Network (CLDN), *Atmos. Meas. Tech. Discuss.*, 3, 1861-1887.
- [26] Rodger, C.J., J.B. Brundell and R.L. Dowden (2005), Location accuracy of VLF World-Wide Lightning Location (WWLL) network: Post-algorithm upgrade, *Annales Geophysicae*, 23, 277-2920.
- [27] Dowden, R.L., J.B. Brundell and C.J. Rodger (2002), VLF lightning location by time of group arrival (TOGA) at multiple sites, *Journal of Atmospheric and Solar-Terrestrial Physics*, 64, 817-830.
- [28] Dowden, R.L., R.H. Holzworth, C.J. Rodger, J. Lichtenberger, N.R. Thomson, A.R. Jacobson, E. Lay, J.B. Brundell, T.J. Lyons, S. O'Keefe, Z.-I. Kawasaki, C. Price, V. Prior, P. Ortega, Y. Weinman, Y. Mikhailov, O. Veliz, X. Qie, G. Burns, A. Collier, O. Pinto, R. Diaz, C. Adamo, E.R. Williams, S. Kumar, G.B. Raga, J.M. Rosado, E.E. Avila, M.A. Clilverd, T. Ulich, P. Gorham, T.J.G. Shanahan, T. Osipowicz, G. Cook and Y. Zhao (2008), World-wide lightning location using VLF propagation in the Earth-Ionosphere waveguide, *IEEE Antennas and Propagation Magazine*, 50 (5), 40-60.
- [29] Jacobson, A.R., R.H. Holzworth, J. Harlin, R.L. Dowden and E.H. Lay (2006), Performance Assessment of the World Wide Lightning Location Network (WWLLN), Using the Los Alamos Sferic Array (LASA) as Ground Truth, *J. Atmos. Oceanic Technol.*, 23, 1082-1092.

- [30] Rodger, C.J., J.B. Brundell, R.H. Holzworth and E.H. Lay (2009), Growing Detection Efficiency of the World Wide Lightning Location Network, Am. Inst. Phys. Conf. Proc., Coupling of thunderstorms and lightning discharges to near-Earth space: Proceedings of the Workshop, Corte (France), 1118, 15-20.
- [31] Chisholm, A.J., and J.H. Renick (1972), The kinematics of multicell and supercell Alberta hailstorms, Research Council of Alberta Hail Studies, 72-2, 24-31.
- [32] Levis, C.A., J.T. Johnson and F.L. Teixeira (2010), Radio wave propagation: physics and applications, Imprint: Hoboken, NJ : Wiley.
- [33] Bilitza, D., and B. Reinisch (2008), International Reference Ionosphere 2007: Improvements and new parameters, J. Adv. Space Res., 42, (4), 599-609.
- [34] Lay, E.H., A.R. Jacobson, R.H. Holzworth, C.J. Rodger and R.L. Dowden (2007), Local time variation in land/ocean lightning flash density as measured by the World Wide Lightning Location Network, Journal of Geophysical Research, 112, D13111, 9.
- [35] Yoshida, S., C.J. Biagi, V. Rakov, J.D. Hill, M. Stapleton, D.M. Jordan, M.A. Uman, T. Morimoto, T. Ushio, Z.-I. Kawasaki and M. Akita (2012), The initial stage processes of rocket-and-wire triggered lightning as observed by VHF interferometry, J. Geophys. Res., 117, D09119.
- [36] Jacobson, A.R., and T.E.L. Light (2012), Revisiting "Narrow Bipolar Event" intracloud lightning using the FORTE satellite, Annales Geophysicae, 30, 2, 389-404.
- [37] Bilitza, D., L.-A. McKinnell, B. Reinisch, and T. Fuller-Rowell (2011), The International Reference Ionosphere (IRI) today and in the future, J. Geodesy, 85, 909-920.

- [38] Sen, H. K. and A. A. Wyller (1960), On the generalization of the Appleton-Hartree magnetoionic formulas, *J. Geophys. Res.*, 65(12), 3931–3950.
- [39] Taniguchi, T., A. Hirata, T. Morimoto and Z. Kawasaki (2006), Propagation Characteristic of Wideband Electromagnetic Wave in the Ionosphere, *IEEJ Transactions on Fundamentals and Materials*, 126, 11, 1173-1176.
- [40] Light, T. E. L. and A. R. Jacobson (2002), Characteristics of impulsive VHF lightning signals observed by the FORTE satellite, *J. Geophys. Res.*, 107(D24), 4756.
- [41] Shao, X.-M. and A. R. Jacobson (2002), Polarization observations of lightning-produced VHF emissions by the FORTE satellite, *J. Geophys. Res.*, 107(D20), 4430.
- [42] Lang, T. J., W. A. Lyons, S. A. Rutledge, J. D. Meyer, D. R. MacGorman, and S. A. Cummer (2010), Transient luminous events above two mesoscale convective systems: Storm structure and evolution, *J. Geophys. Res.*, 115, A00E22.
- [43] Rodger, C. J., A. Seppälä, and M. A. Clilverd (2008), Significance of transient luminous events to neutral chemistry: Experimental measurements, *Geophys. Res. Lett.*, 35, L07803.
- [44] Thomas, J. N., B. H. Barnum, E. Lay, R. H. Holzworth, M. Cho, and M. C. Kelley (2008), Lightning-driven electric fields measured in the lower ionosphere: Implications for transient luminous events, *J. Geophys. Res.*, 113, A12306.
- [45] Cummer, S. A. and W. A. Lyons (2005), Implications of lightning charge moment changes for sprite initiation, *J. Geophys. Res.*, 110, A0430.

[46] Sato, M., Y. Takahashi, M. Kikuchi, M. Suzuki, A. Yamazaki, and T. Ushio (2011), Lightning and Sprite Imager (LSI) onboard JEM-GLIMS, IEEJ, Transactions on Fundamentals and Materials, 131, 12, 994-999.

[47] Sato, M., Y. Takahashi, M. Suzuki A. Yamazaki, and T. Ushio (2011), Six-Channel Spectrophotometer (PH) Onboard JEM-GLIMS, IEEJ, Transactions on Fundamentals and Materials, 131, 12, 1000-1005.

[48] Labitzke, K. and H. Van Loon (1997), The signal of the 11-year sunspot cycle in the upper troposphere-lower stratosphere, Space Sci. Rev. 80, 393-410.



# List of Publications

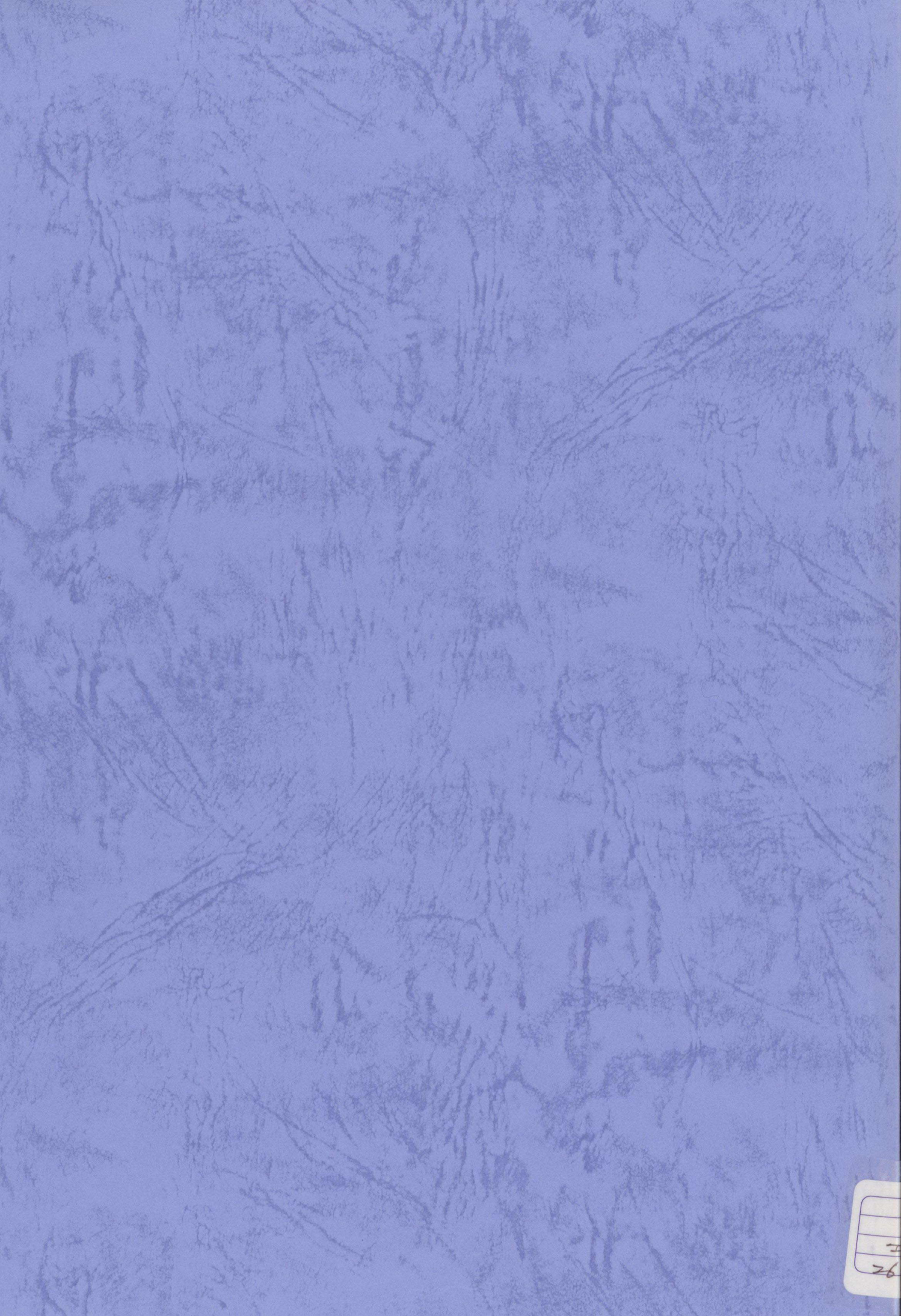
## Journal Papers

- A.1** H. Kikuchi, T. Morimoto, T. Ushio, and Z.-I. Kawasaki (2010), Wideband Radio Wave Observations of Lightning Discharge by Maito-1 satellite, IEICE Transactions on Communications, E93-B, 8, 2226-2227.
- A.2** H. Kikuchi, S. Yoshida, T. Morimoto, T. Ushio, Z.-I. Kawasaki (2011), Satellite Observations for Lightning Discharges and Analysis of VHF Electromagnetic Waveforms, 131, 9, IEEJ. Transactions on Fundamentals and Materials, 705-710.
- A.3** H. Kikuchi, S. Yoshida, T. Morimoto, T. Ushio and Z.-I. Kawasaki, The ionospheric effect on the determination of lightning source location using VHF radio waves by satellite remote sensing (in Japanese), IEEJ. Transactions on Fundamentals and Materials (in press).
- A.4** H. Kikuchi, S. Yoshida, T. Morimoto, T. Ushio and Z.-I. Kawasaki, VHF Radio Wave Observations by Maito-1 Satellite and Evaluation of its Relationship with Lightning Discharges, IEICE Transactions on Communications (in press).

## Proceedings of International Conferences

- B.1** T. Morimoto, H. Kikuchi, T. Ushio, Z.-I. Kawasaki, H. Hashimoto, T. Aoki (2009), Broadband VHF observations for lightning impulses from a small satellite SOHLA-1 (Maito-1), AGU fall meeting 2009, San Francisco, U.S.A., Dec. 2009.
- B.2** T. Morimoto, H. Kikuchi, T. Ushio, and Z.-I. Kawasaki (2010), Space-borne VHF lightning observations by Maito-1 and JEM-GLIMS missions, 2010 Asia-Pacific Radio Science Conference (AP-RASC'10), Toyama, Japan, Sep.r 2010.

- B.3** H. Kikuchi, T. Morimoto, T. Ushio and Z.-I. Kawasaki (2010) ,VHF Broadband Observations of Lightning Discharges by Mado-1 satellite, Proceedings of 2010 Asia-Pacific Radio Science Conference (AP-RASC'10), Toyama, Japan, Sep. 2010.
- B.4** T. Morimoto, H. Kikuchi, T. Ushio, and Z.-I. Kawasaki (2010), Gradual approach to realize lightning monitoring from space by means of VHF observations, AGU fall meeting 2010, San Francisco, U.S.A., Dec. 2010.
- B.5** T. Morimoto, H. Kikuchi, S. Yoshida, T. Ushio and Z.-I. Kawasaki (2011), Toward Space-based VHF Broadband Digital Interferometer for Lightning Observations, the XIV International Conference on Atmospheric Electricity, Brazil, Rio de Janeiro, Aug. 2011.
- B.6** H. Kikuchi, S. Yoshida, T. Morimoto, T. Ushio, and Z.-I. Kawasaki (2011), Propagation characteristics of lightning observed VHF pulses with the Mado-1 satellite, the XIV International Conference on Atmospheric Electricity, Rio de Janeiro, Brazil, Aug. 2011.
- B.7** H. Kikuchi, S. Yoshida, T. Morimoto, T. Ushio, Z.-I. Kawasaki (2012), VHF observations on lightning discharges from a small satellite and the International Space Station, AGU fall meeting 2012, San Francisco, U.S.A., Dec. 2012.



26